Sensors & Actuators: B. Chemical 272 (2018) 369–392

Contents lists available at ScienceDirect

Sensors and Actuators B: Chemical

journal homepage: www.elsevier.com/locate/snb

2D metal oxide nanoflakes for sensing applications: Review and perspective

A. Petra Dral, Johan E. ten Elshof*

Inorganic Materials Science, MESA+ Institute for Nanotechnology, University of Twente, P.O. Box 217, 7500 AE Enschede, The Netherlands

ARTICLE INFO

Keywords:
Two-dimensional
Metal oxide
Nanosheet
Biosensor
Gas sensor
Hierarchical architecture

ABSTRACT

In this review the state of the art and future prospects of 2-dimensional (2D) metal oxide nanoflakes used as active sensing elements for the detection of solutes, gases and radiation are discussed. 2D material geometries are particularly interesting for sensing applications because they provide large specific surface areas and are suitable for crystal facet engineering. In addition, unique material properties of atomically thin nanosheets due to quantum size effects provide engineering possibilities beyond the realm of their bulk counterparts. A variety of possibilities in materials, synthesis routes, (hierarchical) sensor architectures and application areas is sketched. The discussion is focused on high-performing sensors and innovative concepts. The scope is limited to nanoflakes with a thickness of up to 50 nm. Special attention is given to sensing based on material properties that are unique to atomically thin nanosheets.

1. Introduction

Many industries and day-to-day technologies rely on sensors for safety, quality control and analysis. Sensors are required to detect i.e. specific gases, biomolecules or radiation with sufficient sensitivity, selectivity, speed and stability ('4S' requirements). Using 2D sensing elements has several advantages as opposed to using bulk 3D units of the same material. Freestanding 2D nanoflakes have a large specific surface area, which enables extensive interaction with the environment even for small amounts of material. Also, rigid 2D building blocks can facilitate an open packing in 3D assemblies when they are immobilized in a non-stacking fashion. In comparison with 3D architectures derived from 1D or 0D components, 2D-in-3D architectures can provide more efficient electron transport because of fewer grain boundaries and they also tend to have a better mechanical stability [1,2]. Using 2D subunits furthermore allows tuning of the surface reactivity and selectivity via crystal facet engineering [1,3,4]. In addition, unique material properties of atomically thin nanosheets due to quantum size effects, e.g. the increased band gap energy of TiO_2 nanosheets [5] and the visible light absorption of MnO_2 nanosheets [6], provide engineering possibilities beyond the realm of their bulk counterparts. To date, literature reports occasionally describe such unique intrinsic material properties for metal oxide-based sensing, but most often the 2D concept is interpreted only from a geometric viewpoint (increased surface area).

In the past year many reviews have been published on a variety of 2D materials for sensing applications. Zhang et al. [7], Bo et al. [8], Campuzano et al. [9], Zhang et al. [10], Fu et al. [11] and Xu et al. [12] reviewed 2D graphene-based sensors, mostly employing electrochemical mechanisms and for biological applications. Wang et al. did the same and also included 2D transition metal dichalcogenides, graphite carbon nitride and boron nitride [13]. Bollella et al. furthermore included 2D transition metal oxides [14]. A review focusing on 2D transition metal dichalcogenides for sensors was published by Ping et al. [15]. Yang et al. [16] and Liu et al. [17] published a review focusing on gas sensors, describing various sensor devices and synthetic methods and including 2D graphene-based materials, metal (di)chalcogenides, phosphorene, boron nitride, MXenes and metal oxides. Given the yearly number of publications on 2D metal oxides as sensing elements, indicated in Fig. 1, the present review is devoted particularly to 2D metal oxide sensors. The classification in gas, solute and radiation sensors reflects the available literature and was not used to limit the literature search.

The present review discusses the state of the art and future prospects of 2D metal oxide nanoflakes used as active sensing elements. Most of the publications on 2D metal oxide sensors are proof-of-concept reports demonstrating a variety of possibilities without yet reaching competitive performances. These studies will be summarized shortly to sketch the variety of possibilities in materials, synthesis routes, (hierarchical) sensor architectures and application areas. The discussion is focused on highly sensitive sensors and innovative concepts. Notes on sensor selectivities are included as well, but sensor speed and stability (other '4S' requirements) are left out of scope. Special attention is given to sensing based on material properties that are unique to atomically thin nanosheets. The outline of this review is as follows. In Section 2 a variety

* Corresponding author.
E-mail addresses: a.p.dral@alumnus.utwente.nl (A.P. Dral), j.e.tenelshof@utwente.nl (J.E. ten Elshof).

https://doi.org/10.1016/j.snb.2018.05.157
Received 18 January 2018; Received in revised form 18 May 2018; Accepted 26 May 2018
Available online 31 May 2018
0925-4005/

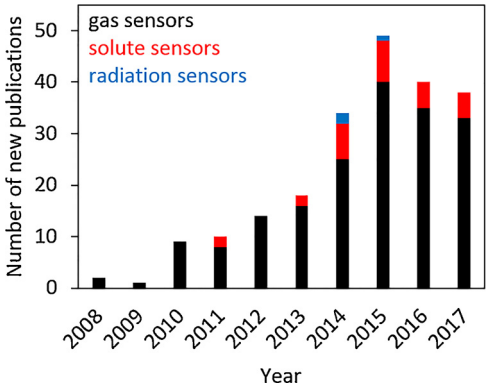

Fig. 1. Indication of the number of new publications per year on sensors with 2D metal oxide nanoflakes of up to 50 nm thick as active sensing elements. The numbers are based on the literature references in Table 1 and 4 and Section 5.

of 2D-based metal oxide architectures and synthesis routes is introduced and described. In Section 3 the use of 2D metal oxide nanoflakes for sensing of solutes is discussed, including sensing mechanisms, used materials and reported sensor performances. The same aspects are discussed for 2D metal oxide nanoflakes for gas sensing in Section 4, with specific attention for rational design approaches. In Section 5 2D metal oxide nanoflakes for sensing of radiation are discussed. In Section 6 a perspective is given on future development and optimization of sensor devices.

2. 2D-based architectures and their synthesis

2.1. Architectures

2D nanoflakes can be employed as active sensing elements both individually and incorporated in 3D architectures. Individual nanoflakes are difficult to handle and are thus mostly employed for sensing in suspended form to detect solutes. Examples of a few-nm thin flexible nanoflake and a stack of rigid nanoflakes of 10–15 nm thickness are shown in Fig. 2a–b [18,19]. The majority of reports employing 2D nanoflakes as active sensing elements do so by incorporating the nanoflakes in porous 3D architectures. This ensures good exposure of the 2D surfaces to the environment with proper gas diffusion through the assembly. The most common architectures are flower-like structures as shown in Fig. 2c–d [20,21], in which the nanoflakes form a highly porous sphere and are oriented perpendicular to the sphere surface, i.e. emanating from the core. The nanosheets may self-assemble spontaneously or can grow on pre-existing cores. In the tree-like structures of Fig. 2e [22] the nanoflakes are standing on the outer surface of nanorods or tubes (trunks). Nanoflakes vertically standing on a flat substrate form nanowalls as in Fig. 2f [23]. Densely packed nanowalls or randomly oriented nanoflakes can be categorized as nanoforests, shown in Fig. 2g [24]. Films included in this review are not continuous but consist of 2D subunits (crystallites), i.e. layers of nanoflakes that horizontally cover a flat substrate or layers of aggregated nanoflakes without a particular order. The difference between walls, forests and films is somewhat arbitrary. In general it is important that gas molecules can easily diffuse to the active surface, i.e. too densely packed architectures may lose effectiveness.

2D nanoflakes in 3D assemblies generally require a thickness of several nm or more in order to have sufficient mechanical strength to sustain an open architecture under dry conditions. This is usually achieved via bottom-up syntheses and can yield continuous single crystals, but 2D nanoflakes may also consist of 0D [25,26] or 1D [27,28] subunits. Meso- and macropores can be created in the nanoflakes e.g. by a loose connection of 0D subunits [26] or during oxidation or annealing of non-porous precursor nanoflakes [29–31]. Scanning electron microscopy and transmission electron microscopy images of 2D nanoflakes with meso- and macropores are shown in Fig. 3 [2,32]. Porosity facilitates diffusion of target species in the sensing architecture and can increase the surface area.

2.2. Synthesis of 2D nanoflakes

The majority of the 2D nanoflakes is synthesized via hydrothermal or solvothermal procedures. Common advantages of hydrothermal and

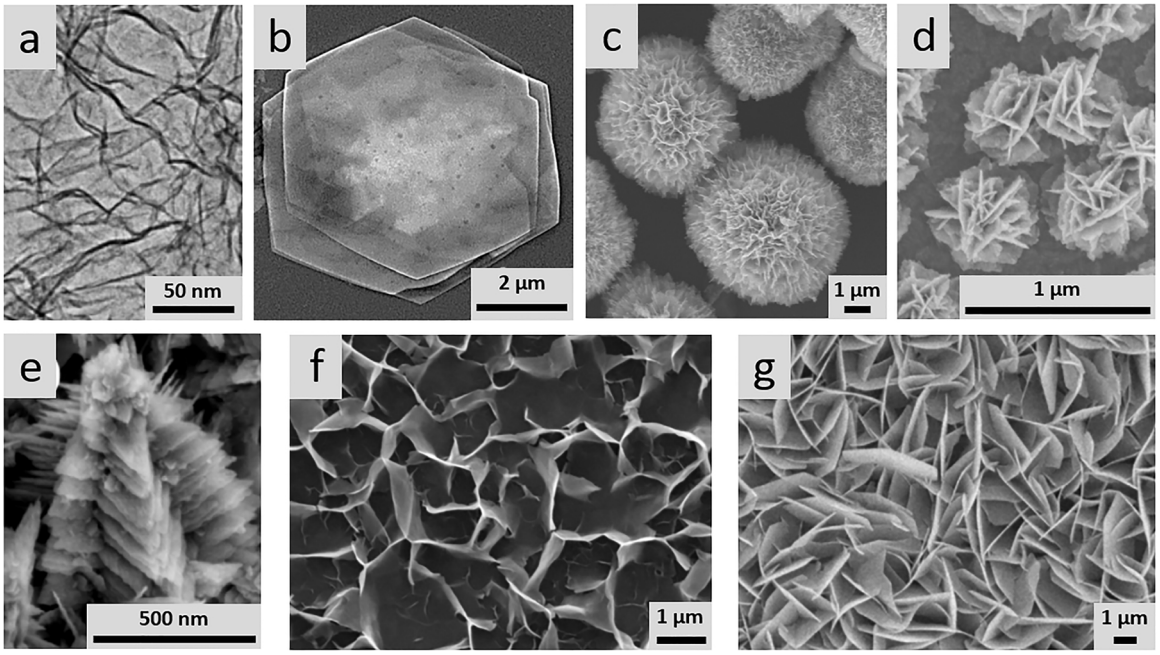

Fig. 2. Transmission electron microscopy image (a) and scanning electron microscopy images (b-g) of individual and assembled nanoflakes. (a) Flexible nanoflake. Reprinted from [18] with permission from Elsevier. (b) Stack of rigid nanoflakes. Reprinted with permission from [19]. Copyright 2014 American Chemical Society. (c,d) Flower-like assemblies. Reprinted from [20,21] with permission from Elsevier and Springer. (e) Tree-like assembly. Reprinted from [22] with permission from Elsevier. (f) Walls. Reprinted from [23] with permission from Elsevier. (g) Forest. Reprinted from [24] with permission from Elsevier.

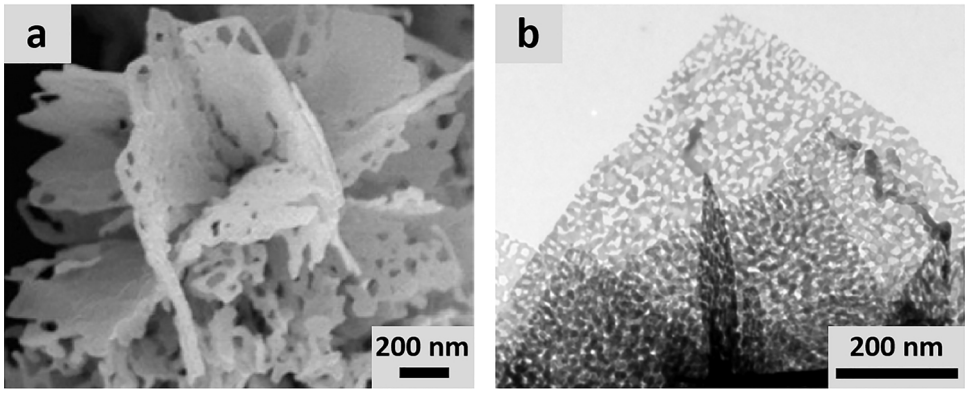

Fig. 3. (a) Scanning electron microscopy image of meso- and macropores in 2D nanoflakes of SnO_2. Reprinted from [32] with permission from Elsevier. (b) Transmission electron microscopy image of mesopores in 2D nanoflakes of SnO_2. Reprinted from [2] with permission from Elsevier.

solvothermal syntheses are simplicity, scalability, low costs, low processing temperatures and compatibility with flexible substrates. Metal oxide precursors are dissolved in water or an organic solvent and the reaction typically takes place at temperatures of 75–200 °C with reaction times of 3–12 h, sometimes extended up to a few days. Common precursors are e.g. metal chlorides, sulfates, nitrates and acetates. For 2D-in-3D hierarchical architectures, the metal oxide may grow in the desired structure spontaneously [33–37] or structure-directing agents such as cetyltrimethylammoniumbromide [38–41], glycerol [39,42], hexamethylenetetramine [23,43–45], polyvinylpyrrolidone [2,40,46,47], urea [25,40,48,49], sodiumdodecylsulfate [50–52] or polyethyleneglycol [52–55] can be added. Also, seed layers may be employed to initiate growth [23,24,43,44,56] and occasionally microwave-assisted procedures are used [57,58]. After the 2D-in-3D architecture is obtained, annealing at 250–500 °C may be required for decomposition of organic residues, dehydroxylation or crystallization. Procedures without annealing are also possible [35,53,59,60]. In some cases the 3D architecture is obtained for sulfide intermediates such as In_2S_3, MoS_2 or SnS_2, which are then converted into the corresponding metal oxide by thermal oxidation [29,61,62]. An uncommon type of hydrothermal fabrication has been reported for $ZnSnO_3$ structures, involving the hydrothermal dissolution of 3D cubes and subsequent recrystallization into 2D nanoflakes [63].

Alternative synthesis approaches include room-temperature solution procedures, reported for e.g. ZnO [64–66] and MnO_2 [38,67]. Room-temperature sonochemical procedures followed by thermal annealing have been reported for flowers of WO_3 [68] and Fe_2O_3—NiO [69]. The WO_3 flowers were synthesized from Na_2WO_4 in aqueous solution with oxalic acid as capping agent, while the Fe_2O_3—NiO flowers were derived from a coordination polymer precursor with polyethyleneglycol as surfactant. Coordination polymer precursors provide an easy route to multicomponent mixed metal oxides with high composition uniformity [69,70]. Electrodeposition has been reported as a method to prepare Ni flowers that can subsequently be oxidized to NiO [21,71]. ZnO nanoforests and TiO_2 nanowalls have been obtained by oxidation of corresponding metal films [72,73]. 2D metal oxide nanoflakes of only a few nm thickness can be obtained by chemical exfoliation from layered parent compounds, reported for e.g. 1 nm thick RuO_2 [74], 4 nm thick MoO_3 [75–77] and WO_3 [78]. Exfoliation can be assisted by e.g. mild mechanical shaking or sonication and the nanoflakes can be used individually in suspension or be processed into films. More elaborate descriptions of the exfoliation of 2D metal oxides can be found elsewhere [17,79].

The synthesis route determines whether the formed 2D nanoflakes are single-crystalline or polycrystalline and this can profoundly influence the sensor performance. Crystal grain boundaries contain large numbers of surface states that can trap or scatter free charge carriers, which increases the effective resistivity [80]. Single crystalline nanoflakes tend to have better stability at elevated temperatures due to reduced grain coalescence and resulting alterations of grain boundaries and porosity [81]. Other important synthesis aspects are the obtained crystal orientation and surface morphology, as discussed extensively elsewhere [82]. 2D geometries are particularly suitable for crystal facet engineering.

3. 2D nanoflakes for solute sensing

3.1. Sensing mechanisms

For sensing of solutes, 2D nanoflakes can be immobilized on a support or be used in suspended form. Nanoflakes in suspension can function as individual sensors even if they are only a few atoms thick. Target species in solute sensing are often biomolecules, which can be immobilized onto nanoflakes via e.g. non-specific Van der Waals forces and electrostatic interactions. Sensing based on non-specific interactions is not favorable when analyzing mixtures of biomolecules. In contrast, very high selectivities can be reached for nanoflakes decorated with signaling moieties that interact with the target molecules via e.g. DNA or peptide recognition [38,83,84]. Adsorption-based sensing of solutes often only involves turn-on sensing; once the target molecules are bound by the sensing platform, they do not detach spontaneously anymore. If the nanoflakes are immobilized on a support, regeneration may be possible to enable reuse of the sensor.

Adsorption events can be detected via e.g. fluorescent, plasmonic and/or chemiresistive signals. In fluorescent sensors, light-absorbing metal oxides generally quench the fluorescence of adsorbed signaling species. Upon interaction of the signaling species with the target molecule, e.g. via DNA hybridization, the signaling species (partially) desorbs and the dye label escapes from the quenching influence of the metal oxide nanoflakes, thus retaining its fluorescence [38,83,84]. Alternatively, the fluorescent signaling species can be released via consumption of the metal oxide nanosheets in oxidation reactions with the target species [67,85].

Plasmonic sensors exploit the sensitivity of surface plasmons in metal oxide nanoflakes towards electrical interactions with adsorbed species. The adsorption of charged species causes a change in the free electron density at the surface of the metal oxide, which affects the intensity of plasmonic absorption [75]. Plasmonic sensing particularly benefits from 2D sensing elements, because the existence of one large depolarization factor in 2D geometries reduces the plasmon resonance wavelength as compared to 1D geometries that have two modest depolarization factors [75]. This can shift the resonance wavelength into the visible light and infrared region, which is important for applications as these wavelengths are commonly used in optical systems [75]. A

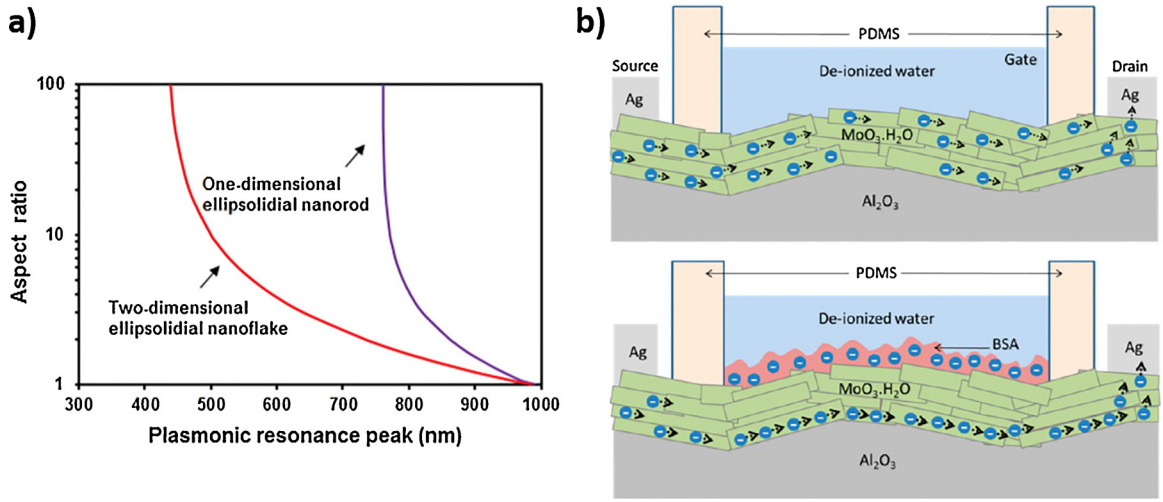

Fig. 4. (a) Theoretical relation between the aspect ratio and plasmonic resonance peak wavelength for 2D and 1D geometries of similar stoichiometry. The relations are based on the Mie-Gans theory, see the supplemental information of [75] for equations and further details. Reprinted with permission from [75]. Copyright 2014 WILEY-VCH Verlag GmbH & Co. (b) Schematic representation of FET sensing of BSA with 2D MoO_3 nanoflakes. Reprinted with permission from [86]. Copyright 2013 American Chemical Society.

schematic representation of the theoretical relation between the aspect ratio and plasmonic resonance peak wavelength for 2D and 1D geometries of similar stoichiometry is shown in Fig. 4a [75].

An example of field-effect transistor (FET) solute sensing employing a film of 2D metal oxide nanoflakes as conduction channel is given in Fig. 4b [86]. The electrical conductivity of the channel varies with the adsorption of target molecules on its surface. In Fig. 4b the adsorption of negatively charged bovine serum albumin (BSA) molecules creates a negative potential on the surface of the n-type semiconductor MoO_3 nanoflake film, which increases the channel resistance.

As an alternative to adsorption-based sensing, solutes may also be detected via electrochemical reactions. Oxidation or reduction of the target species at a nanoflake-covered electrode yields an electric current or potential as response. Electrochemical sensors are especially employed for glucose detection. Drawbacks of commonly used glucose sensors based on enzymes are their poor stability, high cost and weakness to environmental conditions [87], which can be circumvented by non-enzymatic electrochemical sensing.

3.2. Materials

An overview of literature reports on 2D metal oxide nanoflakes that have served as active sensing element for solutes is given in Table 1, indicating the used materials, architectures, syntheses, 2D thicknesses, target species and underlying sensing mechanisms. Individually suspended 2D nanoflakes for sensing generally have a layered structure with a thickness of only a few unit cells. An advantage of layered structures is the possibility of ionic intercalation, which allows very high dopant concentrations (ultradoping) [75]. Ultradoping can increase the free carrier concentration in semiconductors to such an extent that plasmonic resonances shift towards the near-infrared and visible light regions [88]. Metal oxides suitable for plasmonic sensing are e.g. 2D MoO_{3-x} and WO_{3-x}, both of which benefit from having large dielectric constants and are capable of accommodating ultradoping [75,76,89]. For few-nm MoO_3 nanoflakes, irradiation with solar light in the presence of water causes intercalation of the layered structure with H^+ ions and partially reduces Mo. This results in more oxygen vacancies and causes a transition from semiconducting α-MoO_3 to metallic Mo_4O_{11}. Fig. 5 shows UV/visible light absorption spectra of 2D MoO_3 nanoflakes before and after solar light irradiation, demonstrating the appearance of an absorption band in the near-infrared/visible light region that blue-shifts with increasing irradiation time [75].

Fluorescent sensors require light-absorbing materials such as MoO_3 and MnO_2 [38,67,83,84] to quench the fluorescence of the signaling species. Most 2D transition metal oxides show intensive light absorption due to strong *d-d* transitions [109]. Metal oxides can be beneficial for fluorescent sensing as compared to metal sulfides and selenides because the oxygen atoms yield stronger electrostatic interactions with the signaling species, which causes closer proximity and more efficient quenching [84]. An advantage of atomically thin MnO_2 nanoflakes is that they are also strongly oxidative towards organic compounds and this feature can be employed in combination with their light absorption [67,85].

Electrochemical sensors require metal oxides that are oxidative or reducing towards the target species. Many 2D transition metal oxides have high isoelectric points, which facilitates the immobilization and subsequent charge transfer for a wide range of biomolecules with lower isoelectric points [109,110]. NiO is used for electrochemical glucose sensors because of its low cost, good electrocatalytic activity, biocompatibility and electron transfer capability [25,100]. The absence of poisoning by oxidation products under alkaline conditions enables repeated usage of NiO-based sensors [111]. Other electrochemically active materials are $Ni(OH)_2$, which is also a precursor for NiO, and CuO and Co_3O_4 [28,90,103,106].

3.3. Performance

3.3.1. Glucose sensors

Most glucose sensors are based on non-enzymatic electrochemical detection with 2D NiO, $Ni(OH)_2$, CuO and Co_3O_4 nanoflakes, of which the performances are summarized in Table 2. The lowest detection limits (< 1 μM) and linear response onsets (1 μM with a window up to several thousand μM) have been reported for $Ni(OH)_2$ sensors [101,103,104]. The highest sensitivity has been reported by Cui et al., reaching over 30 mA mM^{-1} cm^{-2} with flower-like structures of NiO on a core of carbon [25]. The addition of urea, ascorbic acid, L-leucine, L-lysine and NaCl did not significantly interfere with the glucose signal. The widest linear response range has been reported by Ngo et al. using NiO flowers on a film of reduced graphene oxide and decorated with Ag particles [100]. The sensitivity was 1.9 mA mM^{-1} cm^{-2} in the linear response region of 50 μM − 7.5 mM and 116 μA mM^{-1} cm^{-2} in the linear response region of 10–25 mM. No significant interference was observed from uric acid, ascorbic acid, dopamine, fructose, lactose and sucrose. Solute interference can be suppressed not only by tuning the sensor

Table 1
Overview of literature reports on 2D metal oxide nanoflakes that have served as active sensing element for solutes. Syntheses denoted as 'hydrothermal' include at most 50% organic solvent. Syntheses denoted as 'solution' include temperatures up to 45 °C.

Reference	2D metal oxide	Architecture	Synthesis	2D thickness [nm]	Target species	Sensing mechanism
[90]	Co_3O_4	aggregate with $Ni(OH)_2$	solvothermal	5–15	glucose	electrochemical
[28]	CuO	random film of stacked flakes	solution	20–40	glucose	electrochemical
[38]	MnO_2	flower decorated with dye-labeled ssDNA	solution	4	ssDNA	fluorescent
[67]	MnO_2	individual flake decorated with 7-hydroxycoumarin	solution	1	ascorbic acid	fluorescent
[85]	MnO_2	individual flake decorated with protein-stabilized Au nanoclusters	solution	probably 1	glutathione	fluorescent
[83]	MnO_2	individual flake decorated with dye-labeled ssDNA or peptide	solution	probably 1	ssDNA (ochratoxin A), cathepsin D	fluorescent
[91]	MnO_2	individual flake decorated with dye-labeled DNA	solution	1	microRNA	fluorescent
[92]	MnO_2	individual flake on doped $NaYF_4$ nanoparticles	solution	1–3	H_2O_2, glucose	fluorescent
[93]	MnO_2	individual flake on doped $NaYF_4$ nanoparticles	solution	1–3	glutathione	fluorescent
[94]	MnO_2	individual flake on doped $Sr_2MgSi_2O_7$ nanoparticles	solution	probably 1–3	glutathione	fluorescent
[95]	MnO_2	individual flake decorated with C nanoparticles	solution	probably 1–3	glutathione	fluorescent
[96]	MnO_2	individual flake on phenol formaldehyde resin particles	solution	< 5	glutathione	fluorescent
[97]	MnO_2	individual flake decorated with Si quantum dots	solution	probably 1–3	glutathione	fluorescent
[18]	MnO_2	film	solvothermal	5	H_2O_2	electrochemical
[75]	MoO_{3-x}	individual flake	exfoliation	4–6	BSA	plasmonic
[76]	MoO_{3-x}	individual flake	exfoliation	4–26	BSA	plasmonic
[98]	MoO_{3-x}	flower with MoO_3 surface	solvothermal	20–30	methylene blue	plasmonic
[84]	MoO_3	individual flake decorated with dye-labeled ssDNA	exfoliation	probably 1–2	ssDNA (prostate-specific antigen)	fluorescent
[86]	MoO_3	film coated with 1 nm Au	exfoliation	1–3	BSA	FET
[99]	$Na_2Ti_3O_7$	film	hydrothermal	10	Hg^{2+}	electrochemical
[25]	NiO	flower on C core	hydrothermal	30–50	glucose	electrochemical
[100]	NiO	flower on RGO film and decorated with Ag particles	hydrothermal	< 50	glucose	electrochemical
[101]	$Ni(OH)_2$	wall [102] on over-oxidized polypyrrole wires	solution	< 50	glucose	electrochemical
[103]	$Ni(OH)_2$	flower	solvothermal	5	glucose	electrochemical
[104]	$Ni(OH)_2$	hollow flower	hydrothermal	< 50	glucose	electrochemical
[105]	$Ni(OH)_2$	flower aggregated with carbon nanotubes	solution (45 °C)	< 50	glucose	electrochemical
[106]	$Ni(OH)_2$	forest on Ni foam	hydrothermal	30	glucose	electrochemical
[107]	TiO_2	flakes and particles decorating RGO	solvothermal	< 5	dopamine	electrochemical
[108]	ZnO	film decorated with antibodies	solution	20	cortisol	electrochemical

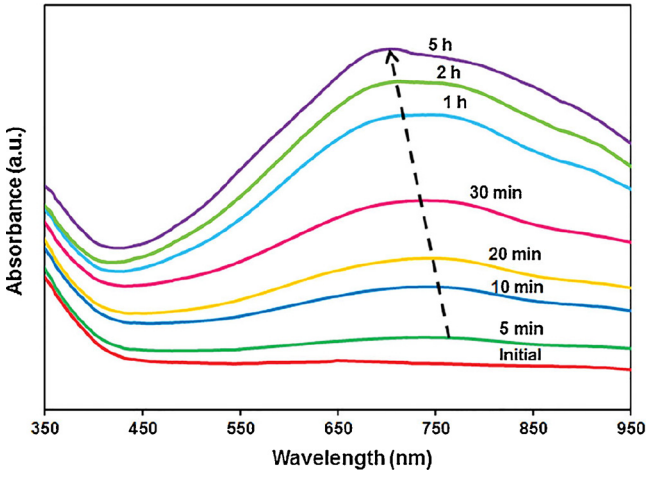

Fig. 5. UV/visible light absorption spectra of 2D MoO_3 nanoflakes before and after solar light irradiation. Reprinted with permission from [75]. Copyright 2014 WILEY-VCH Verlag GmbH & Co.

design, but also by tuning the operation conditions. For example, the operation pH may be chosen such that major interfering species have the same charge as the sensing electrode, i.e. both negative or both positive, and are thus electrostatically repelled [106]. A fluorescent enzymatic glucose sensor employing MnO_2 nanoflakes on doped $NaYF_4$ upconversion nanoparticles has been reported by Yuan et al. [92]. Glucose was degraded by glucose oxidase, which released H_2O_2 that in turn degraded the MnO_2 nanoflakes and thereby restored the fluorescence of the $NaYF_4$ nanoparticles.

Table 2
Sensitivity per cm^2 electrode surface area, lower limit of detection (S/N = 3) and concentration window of linear response for glucose sensors with 2D metal oxide sensing elements.

Reference	2D metal oxide	Sensitivity [$\mu A\,mM^{-1}\,cm^{-2}$]	Lower limit of detection (S/N = 3) [μM]	Linear response window [μM]
[90]	Co_3O_4	1089 / 2145	1.08	5–40 / 40–200
[28]	CuO	26.6 ($\mu A\,mM^{-1}$)	5	10–7300
[92]	MnO_2	n.a.	3.7	0–250 / 250–400
[25]	NiO	30190	2	2–1279
[100]	NiO	1869 / 116	2.44	50–7500 / 10000–25000
[101]	$Ni(OH)_2$	1049	0.3	1–4863
[103]	$Ni(OH)_2$	419	0.08	0.87–10530
[104]	$Ni(OH)_2$	223	0.1	0.8749–7781
[105]	$Ni(OH)_2$	238.5	0.5	100–1100
[106]	$Ni(OH)_2$	2617	2.5	2.5–1050

3.3.2. Glutathione sensors

Glutathione sensors are typically based on composites of fluorescent probes and MnO_2 nanoflakes. The MnO_2 nanoflakes act both as fluorescence quenchers and as oxidizing agents; redox reactions with glutathione consume the nanoflakes and thus restore the fluorescence of the probes. This sensing mechanism only provides turn-on signals, but generally shows good selectivity towards glutathione over other biomolecules and electrolytes. Table 3 lists fluorescent probes, detection limits and concentration windows of linear response reported in literature. All detection limits are well below the typical glutathione concentration in cells (0.5–10 mM [112]). The linear response windows can be tuned by changing the concentration of MnO_2 composites, i.e.

Table 3
Fluorescent probe, lower limit of detection and concentration window of linear response for fluorescent glutathione sensors based on 2D MnO_2 nanoflakes.

Reference	Fluorescent probe	Lower limit of detection [μM]	Linear response window [μM]
[93]	Yb- and Tm-doped core – shell $NaYF_4$	0.9	n.d.
[94]	Eu- and Dy-doped $Sr_2MgSi_2O_7$	0.83	0–100
[95]	C nanoparticles	0.022	0.2–600
[85]	BSA-stabilized Au nanoclusters	20	0–500
[96]	phenol formaldehyde resin	0.0076	0–100
[97]	Si quantum dots	0.153	13.3–417

shifting the signal baseline and saturation. Sensing with MnO_2 nanoflakes has been demonstrated in living cells [93,94,97], in human whole blood [95] and in vivo without external excitation [94].

3.3.3. BSA sensors

Bovine serum albumin detection employing individually suspended MoO_{3-x} nanoflakes of 4–6 nm thickness for plasmonic sensing has been reported by Alsaif et al. [75,76]. Initially, response factors of 1.3 and 2.1 were reported for BSA concentrations of 0.15 and 15 mg mL^{-1}, respectively [75]. In following work the response factors were improved to 7 and 24 for BSA concentrations of 0.25 and 10 mg mL^{-1}, respectively [76]. The response factor was found to increase with decreasing lateral flake size and thickness and with decreasing free electron concentration. No data was reported on sensor selectivities. FET-based BSA sensing with drop-cast films of 2D MoO_3 with a 1-1.5 nm Au coating has been reported by Balendhran et al. [86]. The Au coating was added to facilitate charge transfer between film and electrodes and to facilitate the adsorption of BSA. Resistance changes of about 1% and 30% were achieved for concentrations of 1 and 25 mg mL^{-1}, respectively.

3.3.4. Molecular recognition sensors

DNA- or peptide-based molecular recognition of various biomolecules in suspension has been achieved with fluorescent sensors. He et al. have reported the use of MnO_2 nanoflakes of approximately 4 nm thickness that were assembled in flower architectures and decorated with adsorbed dye-labeled ssDNA signaling species [38]. A linear relation between the fluorescence and target molecule concentration was obtained over the range of 0–5 nM with a detection limit of 300 pM. The sensor was demonstrated to be of general applicability by simply changing the signaling probe for molecular recognition. Yuan et al. used single-layer MnO_2 nanoflakes decorated with dye-labeled ssDNA and peptides for the detection of ochratoxin A and cathepsin D, respectively [83]. The response to ochratoxin A was linear in the range of 0.02-2.0 ng mL^{-1} and was > 1000 times larger than the response to its analogues aflatoxin B1 and B2. For cathepsin D detection a linear response was obtained for concentrations of 1–100 ng mL^{-1}. Yang et al. used single-layer MnO_2 nanoflakes decorated with dye-labeled DNA for the detection of microRNA inside living cells [91]. The MnO_2 nanoflakes not only participated in the fluorescence signaling with a linear response between 0 and 100 pM and a detection limit of 1 pM, but also facilitated cell internalization and protected the DNA label against enzymatic degradation. Dhenadhayalan et al. have reported the ultrasensitive detection of ssDNA with MoO_3 nanoflakes for the application of prostate-specific antigen sensing in live cells [84]. A detection limit of 13 pM was reached.

3.3.5. Other sensors

In vivo detection of ascorbic acid was demonstrated by Zhai et al. using single-layer MnO_2 nanoflakes decorated with fluorescent 7-hydroxycoumarin [67]. The oxidation of ascorbic acid consumed the MnO_2 nanoflakes and thus restored the probe fluorescence. Though the oxidation is not selective towards ascorbic acid, the contribution of ascorbic acid was determined by reference measurements in which all ascorbic acid was removed by ascorbic acid oxidase. A linear response was obtained in the range of 0.5–40 μM with a detection limit of 0.09 μM and a sensitivity of 26 μM^{-1}. Hu et al. used MnO_2 nanosheets for electrochemical oxidative sensing of H_2O_2 with a sensitivity of 3261 mA M^{-1} cm^{-2} and linear responses between 25 nM – 2 μM and 10–454 μM [18]. The detection limit was 5 nM, which enabled detection of H_2O_2 released by living cells. The previously discussed fluorescent glucose sensor reported by Yuan et al. also detected H_2O_2, yielding a detection limit of 0.9 μM and linear responses between 0 and 150 μM and 180–350 μM [92].

Vabbina et al. have reported the electrochemical detection of cortisol with antibody-decorated ZnO nanoflakes, exploiting the favorable catalytic activity and charge transfer capability of the ZnO (0001) crystal plane [108]. This study is one of few that explicitly includes crystal facet engineering in sensor design. Yuan et al. have reported the electrochemical detection of Hg^{2+} cations via ion exchange with layered $Na_2Ti_3O_7$ [99]. No interference was observed from Cd^{2+}, Mn^{2+}, Ni^{2+}, Pb^{2+} and Cu^{2+} cations and the detection limit was as low as 0.005 ppb (~25 pM). Tan et al. have reported flowers of MoO_{3-x} with an oxidized surface of MoO_3 that were used for the detection of methylene blue via surface-enhanced Raman scattering (SERS) [98]. The plasmonic MoO_{3-x} core electromagnetically increased the Raman scattering, while the non-plasmonic MoO_3 shell prevented the photocatalytic degradation of the analyte. A detection limit of 0.1 μM was reached, which is high for semiconductor SERS substrates, and the enhancement factor was comparable to values observed for noble metals, i.e. 1.42×10^5. How et al. have reported reduced graphene oxide (RGO) flakes that were decorated with (001)-faceted TiO_2 nanoflakes for the electrochemical detection of dopamine [107]. This study is another example of sensor design based on crystal facet engineering; TiO_2 (001) facets were created because of their higher surface energy and reactivity than TiO_2 (101) facets [113,114]. A linear response was obtained between 2 and 60 μM with a detection limit of 6 μM [107].

4. 2D nanoflakes for gas sensing

4.1. Sensing mechanism

Most metal oxide gas sensors are based on a chemiresistive sensing mechanism. In-depth descriptions of this sensing mechanism can be found elsewhere [115–117], but in short the electrical resistance of a metal oxide sensing unit is related to the ionosorption of oxidative species from the atmosphere on its surface. In oxygen-containing environments O_2 adsorbs on the metal oxide as O_2^-, O^- or O^{2-} and depletes electrons from the metal oxide surface region. This increases the electrical resistance in n-type semiconductor metal oxides and decreases the resistance in p-type semiconductors (hole accumulation). If the target species of a sensor is reducing such as CO, H_2 or various hydrocarbons, the gas molecules are oxidized by the anionic oxygen species at the metal oxide surface and the resulting electrons are injected back into the metal oxide lattice. This again changes the charge carrier density and thus the electrical resistivity of the sensing unit. Operation temperatures of 100–500 °C are generally required to achieve sufficient ionosorption and activation of O_2. If the target species of a sensor is itself oxidative, such as NO_2, no intermediate adsorbents are required and ionosorption of NO_2 directly affects the metal oxide resistivity. Sensing of oxidative species favors lower operation temperatures to suppress competitive O_2 ionosorption. As alternative to this oxygen ionosorption model, chemiresistive sensing can also be described by an oxygen vacancy model [117,118]. This model focuses on changes in the oxygen stoichiometry as a result of reactions between oxygen vacancies and gas molecules. Chemiresistive sensors are not intrinsically selective towards specific target molecules; the electronic

properties of the metal oxide sensing element can be affected by any oxidizing or reducing species and even by merely physisorbed molecules [119].

4.2. Materials

In general, n-type semiconductors provide higher gas responses than p-type semiconductors because of the difference in localization of conductive and resistive regions [115,117]. The ionosorption of oxidative species withdraws electrons from the metal oxide surface and thus creates a resistive electron-depleted shell around the semiconducting core for n-type semiconductors. An applied current will travel primarily through the less resistive core of the particle, but needs to cross a resistive barrier when travelling from one particle to another. This barrier height is sensitive to the number of ionosorbed oxidative species on the metal oxide surface. The sensor sensitivity increases dramatically with the 2D thickness decreasing to below twice the thickness of the electron depletion layer, i.e. with the electrical resistivity of the metal oxide becoming fully surface-dependent. The depletion layer thickness varies with the charge carrier density, band bending and relative permittivity of the metal oxide [120]. For p-type semiconductors the ionosorption of oxidative species creates a conductive hole-accumulated shell around the semiconducting core. Now the applied current will travel primarily along the conductive shell of the particle and is still affected by the amount of ionosorbed surface species, but to a lesser extent than for n-type materials. Also the 2D thickness and the number of interparticle contacts have less influence on the sensitivity of p-type materials. For identical morphologies the response of p-type materials only equals the square root of that of n-type materials [121]. Advantages of p-type materials tend to be their stronger affinity for oxygen, higher catalytic activity and reduced humidity dependence [115,122].

Electronic processes vary significantly with minor changes in chemical composition, stoichiometry and crystal quality. It is generally believed that oxygen vacancies facilitate the formation of oxygen species on the crystal surface and/or offer active sites for gas adsorption [117]. Metal cation defects are important especially in p-type semiconductors, but studies on their role are rare [117,123]. For 2D NiO sensors the sensitivity towards NO_2 has been reported to increase with increasing nickel vacancy concentrations [123]. Although the majority of 2D metal oxide sensors contains only one metal species, multicomponent structures can be obtained via internal doping, external decoration or composite formation. Secondary components can improve the sensor performance e.g. by changing the charge carrier concentration (electronic sensitization) [124], creating *p-n* junctions [125–127] and catalyzing chemical interactions [20] or increasing the adsorbed gas concentration via the spillover effect [128] (chemical sensitization). More information on the physics of multicomponent structures can be found in a review on nanoscale metal oxide-based heterojunctions for gas sensing by Miller et al. [129].

Despite increasing insight, the rational design of gas sensing materials is still hindered by the lack of detailed knowledge on the relation between intrinsic material properties, processing details and their performance. This issue was recently discussed by Zhang et al. in a review on metal oxide semiconductors for gas sensing, sketching the tremendous number of possibilities in material engineering and highlighting efforts on high-throughput material screening for sensor applications [117]. Rational design is especially difficult with respect to the selectivity of chemiresistive gas sensors, which hinders widespread application for the detection of low-concentration and low-reactive targets such as indoor air pollutants (e.g. benzene, xylene, toluene) and breath biomarkers (e.g. H_2S, CO, acetone, NH_3 and NO) [130]. Various examples of suitable catalyst-target gas combinations are given in a review by Woo et al. [130].

An overview of literature reports on 2D metal oxide nanoflakes that have served as active gas sensing element is given in Table 4, listing the used metal oxides, architectures, syntheses, nanoflake thicknesses and molecules towards which the sensing performance was tested. The differentiation between various metal oxides is schematically shown in Fig. 6; the most widely used metal oxides are ZnO, SnO_2, NiO, WO_3 and In_2O_3. All of these materials have a wide band gap, which is beneficial for reducing background signals due to thermally activated conduction. Other advantages include the high dopability of In_2O_3 [20], the low cost and high chemical and thermal stability of SnO_2 [131] and the large exciton binding energy of ZnO [132,133]. Less commonly used metal oxides include Co_3O_4, MoO_3, CuO, Fe_2O_3, Bi_2WO_6, MnO_2, V_2O_5, Cu_2O, RuO_2, Sn_3O_4, TiO_2, V_4O_9, $ZnFe_2O_4$, $ZnSnO_3$ and layered double hydroxides of Mg-Al and Ni-Fe-Al.

4.3. Performance

Among the various types of 2D metal oxide gas sensors, the ones with predominant responses towards NO_2, acetone, ethanol and formaldehyde have been reported most. For each of these gases an overview of reported maximum sensor responses at concentrations up to 200 ppm is given in Fig. 7, together with an indication of which materials are used most (based on the number of publications). Table 5 lists the details of 2D metal oxide sensors with the highest responses for a variety of other target gases. Because of the intrinsically unselective nature of the chemiresistive sensing mechanism (see Section 4.1), many approaches to increase the sensor response towards either NO_2 or acetone, ethanol and formaldehyde will have a qualitatively similar effect on the sensor response towards other oxidizing or reducing target gases, respectively. In this review, the response of gas sensors is defined as the resistance ratio R_{air}/R_{gas} or R_{gas}/R_{air}, depending on the metal oxide (p-type or n-type) and target species (oxidizing or reducing). Literature values based on different definitions were converted to facilitate comparison. Occasionally, reported data is based on a reference atmosphere of N_2 instead of air.

4.3.1. NO_2 sensors

For NO_2 detection the highest responses have been reached with In_2O_3 as 2D sensing materials. Hu et al. have reported In_2O_3 flower architectures that were decorated with PdO particles and reached responses of up to 4080 for 50 ppm NO_2 at the optimal operation temperature of 110 °C [20]. The response towards NO_2 was approximately 2500–4000 times larger than that towards CH_4, H_2, CO and ethanol and gas concentrations down to 500 ppb could be detected. This excellent performance is explained by the catalyzing effect of Pd, which activates the dissociation of both environmental O_2 and targeted NO_2 on the sensor surface. This causes electron depletion in In_2O_3 and thereby increases its electrical resistance. The undoped In_2O_3 sensor reached a maximum NO_2 response of 1310 for 50 ppm, which is still very high as compared to the other metal oxides (see Fig. 7). Another high-performance gas sensor for NO_2 detection has been reported by Liu et al. based on In_2O_3 flower architectures decorated with reduced graphene oxide sheets to create local *p-n* junctions [125]. The highest response was 1337 for 1 ppm NO_2 at 74 °C and the NO_2 response was 20–1000$^+$ larger than the response towards NH_3, H_2S, O_3, SO_2, Cl_2, ethanol and acetone. NO_2 detection was achieved down to a concentration of 10 ppb and room temperature responses of up to 1098 were reached for 1 ppm. Xu et al. have reported pure In_2O_3 flowers with porous petals that reached a room temperature response of 1210 for 1 ppm NO_2 with 30% relative humidity and could detect concentrations down to 50 ppb [156]. NO_2 sensors based on WO_3 flower architectures have been reported by Wang et al., reaching responses of 150–250 for 0.8 ppm NO_2 at 90–120 °C while being able to detect concentrations down to 2–40 ppb [216,217].

The reason for the observed superiority of In_2O_3 as compared to other metal oxides for NO_2 detection is unclear. Hu et al. have proposed the high electrical conductance of In_2O_3 as reason for its popularity in gas sensor development [20]. However, the charge carrier

Table 4
Overview of literature reports on 2D metal oxide nanoflakes that have served as active gas sensing element. All sensors are based on the chemiresistive sensing mechanism unless denoted otherwise with a footnote. Syntheses denoted as 'hydrothermal' include at most 50% organic solvent. Syntheses denoted as 'solution' include temperatures up to 45 °C. The molecules towards which the sensors showed the highest responses are indicated with 'X' or listed in underlined text. Other molecules towards which the response was tested are indicated with ' + ' or listed in plain text.

Reference	2D metal oxide	Architecture	Synthesis	2D thickness [nm]	methanol	ethanol	propanol	butanol	formalde-hyde	acetone	benzene	toluene	xylene
[134]	AlOOH	film decorated with Co_3O_4 particles	exfoliation	< 5?		+							
[135]	Bi_2WO_6	flower	hydrothermal	10–20	+	X					+		
[136]	Bi_2WO_6	flower	hydrothermal	< 50									
[137]	CdO-ZnO	flower	hydrothermal	20–40	+	X	+			+	+		
[43]	Co_3O_4	wall on carbon foam	hydrothermal	20	+	X			+	+		+	
[138]	Co_3O_4	flower	solvothermal	20–25		+			+	+	+		X
[139]	Co_3O_4	flower with hollow core and decorated with Pd particles	solvothermal	13		+			+		+	X	X
[140]	Co_3O_4	flower	solvothermal	50		X							
[141]	Co_3O_4	film	hydrothermal	20		X							
[142]	Co_3O_4	film	solvothermal	30	+	+				X		+	+
[143]	Co_3O_4	film	hydrothermal	20						X			
[144]	Co_3O_4	film	hydrothermal	< 30									
[127]	CoO-SnO-SnO_2	flower	hydrothermal	5–10	+	X	+		+	+	+		
[145]	CuO	flower	solvothermal	50	+	X			X	X			+
[146]	CuO	flower	solvothermal	50		X							
[147]	CuO	film	hydrothermal	20–25		X				X			
[148]	CuO	film	solution	< 50									
[41]	Cu_2O	flower	hydrothermal	5–10									
[149]	Fe_2O_3	rod-shaped flower with hollow core	solution	3	+	X				X			
[150]	Fe_2O_3	flower	solution (40 °C)	40		X							
[69]	Fe_2O_3—NiO	flower	sonochemical	20–30	X	X	X		X	X	X		
[151]	Fe_2O_3-ZnO	film	solvo-thermal + atomic layer deposition	30–50		+	+			+			
[20]	In_2O_3	flower decorated with PdO	hydrothermal	10–30		+							
[125]	In_2O_3	flower decorated with RGO sheets	hydrothermal	20–40		+				+			
[152]	In_2O_3	flower doped with Ce	hydrothermal	15–20	X	X	X		+	X	+	+	+
[51]	In_2O_3	flower decorated/ doped with MoO_3/Mo	hydrothermal	25	+	X							
[153]	In_2O_3	flower	hydrothermal	20–40	+	X			+	+	+		
[154]	In_2O_3	flower	hydrothermal	20–40	+	+			X	+	+	+	
[29]	In_2O_3	flower	hydrothermal + oxi-dation	10–15	X				+			+	
[155]	In_2O_3	flower	solvothermal	20		+							
[156]	In_2O_3	flower	hydrothermal	15–30		+							
[157]	In_2O_3	flower	solvothermal	10	+	X				+			
[27]	In_2O_3	flower	hydrothermal	10–20		+							
[158]	In_2O_3	forest	solvothermal + flame spraying	4									
[26]	In_2O_3	random film of stacked flakes	solvothermal	20–40	+	+			+			+	
[159]	Mg-Al LDH	flower	hydrothermal	20–30									

(*continued on next page*)

Table 4 (*continued*)

Reference	2D metal oxide	Architecture	Synthesis	2D thickness [nm]	methanol	ethanol	propanol	butanol	formalde-hyde	acetone	benzene	toluene	xylene
[160]	MnO_2	forest decorated with Pd	sputtering	30–40									
[161]	MnO_2	film	solution	few nm	+	+				+		+	
[47]	MoO_3	flower	hydrothermal	10–20		X							
[162]	MoO_3	flower	hydrothermal	15–18		X							
[61]	MoO_3	flower	hydrothermal + oxi-dation	5–10	+	X				+			
[77]	MoO_{3-x}	film coated with 1 nm Au/Pd	exfoliation	4									
[163]	MoO_3	film	exfoliation	1–2	+	X				+	+		
[164]	MoO_3	film	exfoliation	1–2									
[165]	Ni-Fe-Al LDH	flower	hydrothermal	20–30									
[23]	NiO	wall on RGO film	hydrothermal	20–30									
[40]	NiO	flower	hydrothermal, solvothermal	13–32		X							
[34]	NiO	flower	solvothermal	30	+	+			X	+	+	+	
[39]	NiO	flower	hydrothermal	15–25		X							
[33]	NiO	wall	hydrothermal	14		+			+	+			
[48]	NiO	flower on RGO sheet	hydrothermal	10–15									
[36]	NiO	flower	solvothermal	10	+	X			+	+	+	+	
[126]	NiO	tree on ZnO trunk	hydrothermal	30–40	+	+				X			
[132]	NiO	wall with ZnO nanorods	hydrothermal	10–30									
[166]	NiO	flower	hydrothermal	20		X							
[167]	NiO	flower	solvothermal	10–20		X							
[50]	NiO	flower	hydrothermal	10–20		X							
[46]	NiO	flower	hydrothermal	15		X							
[168]	NiO	flower	hydrothermal	15		X							
[21]	NiO	flower	electrodeposition	20	X	X				X			
[58]	NiO	flower decorated with Fe_2O_3	solvothermal	< 5	X	X			+			+	
[169]	NiO	flower doped with Sn	hydrothermal	< 20	+	+			+	+	+		X
[45]	NiO	flower with hollow core and W doping	solvothermal	50	+	+			+	X	+		
[71]	NiO	flower	electrodeposition	20–25		X			+			X	
[170]	NiO	flower decorated with Fe_2O_3 rods	solvothermal	12	+	+			+	+		X	
[171]	NiO	flower	hydrothermal	30	+	X	+		+	+			
[172]	NiO	flower	solution	< 5	+	X				+		+	
[173]	NiO	flower doped with Cr	solvothermal	4–8		+			+		+	X	X
[174]	NiO	flower with hollow core and decorated with Pd/PdO	solution	< 20									
[175]	NiO	film/forest	hydrothermal	30		X							
[176]	NiO	film doped with Al	solvothermal	1–2									
[177]	NiO	film	electrochemical	1–15					X		+	+	
[178]	NiO	film	hydrothermal	20		+				+	+		
[123]	NiO	film	hydrothermal	< 50									
[179]	NiO-ZnO	flower	hydrothermal	5–10		X							
[180]	NiO-WO_3	film	hydrothermal	< 40									
[74]	RuO_2	film	exfoliation	1									
[2]	SnO_2	flower	hydrothermal	20–30		X							

(*continued on next page*)

Table 4 (*continued*)

Reference	2D metal oxide	Architecture	Synthesis	2D thickness [nm]	methanol	ethanol	propanol	butanol	formalde-hyde	acetone	benzene	toluene	xylene
[181]	SnO_2	flower	hydrothermal	5–15	+	X				+	+	+	
[182]	SnO_2	flower decorated with PdO	solvothermal	10					+	+	+	X	
[183]	SnO_2	flower decorated with Fe_2O_3 particles	hydrothermal	20–40	+	+				X			
[184]	SnO_2	flower	hydrothermal	20–30		X							
[22]	SnO_2	tree	hydrothermal	10–20	+	+			X	+	+	+	
[185]	SnO_2	flower	hydrothermal	10–20		X							
[57]	SnO_2	flower decorated with Pd particles	hydrothermal	10–20									
[54]	SnO_2	flower	hydrothermal	30		X							
[186]	SnO_2	flower doped with Cu	hydrothermal	18	+	+				X			
[187]	SnO_2	flower	hydrothermal	35–75		+				X			
[188]	SnO_2	flower	solution	20		X							
[189]	SnO_2	flower	hydrothermal	20	+	+			+	X			
[32]	SnO_2	flower	hydrothermal	20		+				+			
[190]	SnO_2	flower	hydrothermal	25–62		X							
[191]	SnO_2	flower	hydrothermal	10–15		X							
[192]	SnO_2	flower	hydrothermal	10–20	+	X				+			
[193]	SnO_2	flower	hydrothermal, solvothermal	9		+				+			
[194]	SnO_2	flower doped with Zn	hydrothermal	20		+				+	+		+
[195]	SnO_2	flower decorated with rods	hydrothermal	35		X				X		+	
[55]	SnO_2	flower	hydrothermal	< 50		X							
[196]	SnO_2	flower doped with Zn	hydrothermal	30	+	X			+	+		+	
[197]	SnO_2	flower	hydrothermal	6–45	+	+		X		+	+		
[3]	SnO_2	flower doped with Sn^{2+}	hydrothermal	20–30		+				+			
[198]	SnO_2	flower	hydrothermal	50		X							
[199]	SnO_2	flower on $ZnSnO_3$ core	hydrothermal	25	+	X			+	+	+	+	
[200]	SnO_2	flower	hydrothermal	15	+	X			+	+		+	
[62]	SnO_2	flower	hydrothermal + oxi-dation	10						X			
[131]	SnO_2	flower doped with Zn	hydrothermal	20–40		+				+	+		+
[201]	SnO_2	flower decorated with Au particles	hydrothermal	10–20	+	+	+	X		+			
[202]	SnO_2	film decorated with Au particles	hydrothermal + oxi-dation	50		X			+	+			
[203]	SnO_2	forest	hydrothermal	< 20		X							
[204]	SnO_2	forest	hydrothermal	10		X							
[205]	SnO_2	film	hydrothermal	15		X							
[206]	SnO_2	film	hydrothermal	10	+	X	+		+	+		+	+
[59]	Sn_3O_4	flower	hydrothermal	8–15		X							
[73]	TiO_2	wall decorated with SnO_2 particles	oxidation	20–30						X			
[207]	V_2O_5	flower	solvothermal	10–30	+	+	+	+	+	+			
[208]	V_2O_5	film	hydrothermal	2–3									
[35]	V_4O_9	flower	solvothermal	1–2 (?)	X[a]								
[37]	WO_3	flower	hydrothermal	25–40	+	+		+		X		X	
[56]	WO_3	flower	hydrothermal	20–40									
[209]	WO_3	flower	hydrothermal	10–30		X							

(*continued on next page*)

Table 4 (*continued*)

Reference	2D metal oxide	Architecture	Synthesis	2D thickness [nm]	methanol	ethanol	propanol	butanol	formalde-hyde	acetone	benzene	toluene	xylene
[210]	WO_3	flower doped with Co	solvothermal	20–80		+	+			X			
[211]	WO_3	flower	hydrothermal	20–30		X			+				
[212]	WO_3	flower	hydrothermal	20		X							
[213]	WO_3	flower	hydrothermal	40–80	+	X			+	+	+	+	
[214]	WO_3	flower	hydrothermal	15–30									
[215]	WO_3	flower with hollow core	hydrothermal	50–70		+				+			
[216]	WO_3	flower	solution (40 °C)	20–30		+				+			
[217]	WO_3	flower	hydrothermal	30–60		+				+			
[218]	WO_3	flower	solvothermal	10–20		X							
[219]	WO_3	forest	hydrothermal	25		X							
[68]	WO_3	flower	sonochemical	10–20									
[220]	WO_3	flower	hydrothermal	< 50	+	+				+	+	+	
[221]	WO_3	forest	solvothermal	6									
[222]	WO_3	forest	electrochemical	10–50									
[223]	WO_3	film	hydrothermal	10		+							
[78]	WO_3	film	exfoliation	< 10	+	+	+	X					
[224]	WO_3	film	solution	10–30									
[225]	WO_3	film	hydrothermal	10									
[226]	WO_3	film decorated with Pd particles	solution (30 °C)	2–3									
[42]	$ZnFe_2O_4$	flower with hollow core	solvothermal	20	+	+			+	X	+	+	
[60]	ZnO	flower	hydrothermal	43		X		+					
[49]	ZnO	flower	hydrothermal	< 50		X			+	+	+	+	
[30]	ZnO	flower	solution	30–40		+			X	+	+	+	
[227]	ZnO	flower	hydrothermal	20–30		X				X			
[52]	ZnO	flower	hydrothermal	5–10		X			+		+		
[228]	ZnO	flower	hydrothermal	30	+	+			+	X		+	
[229]	ZnO	flower decorated with rods	hydrothermal	30–50	+	+			+		+		
[230]	ZnO	flower	hydrothermal	20–50		X				X	+		
[64]	ZnO	flower	solution	50	+	X	+			+			
[31]	ZnO	flower	hydrothermal	40–50	+	X				+			
[231]	ZnO	flower	hydrothermal	< 50	X	X							
[232]	ZnO	flower	hydrothermal	10–40		X					+		
[53]	ZnO	flower	hydrothermal	20–40		X							
[233]	ZnO	flower	solvothermal (microemulsion-based)	20–30		+			+	+			
[234]	ZnO	film	hydrothermal	18		+					+	+	
[235]	ZnO	flower and sheet/ aggregate	hydrothermal	50		X			+	+			
[65]	ZnO	flower decorated with In_2O_3 particles	solution	30–50					X				
[66]	ZnO	flower decorated with $Pd_{0.5}Pd_3O_4$ particles	solution	30–40	X								
[236]	ZnO	flower decorated with Ag particles and mixed with RGO sheets	hydrothermal	6									
[236]	ZnO	flower	hydrothermal	6									
[237]	ZnO	flower	hydrothermal	5–10?						X			

(*continued on next page*)

Table 4 (*continued*)

Reference	2D metal oxide	Architecture	Synthesis	2D thickness [nm]	methanol	ethanol	propanol	butanol	formalde-hyde	acetone	benzene	toluene	xylene
[238]	ZnO	flower	hydrothermal	10–20		X							
[124]	ZnO	flower doped with Fe	hydrothermal	30					X		+	+	
[239]	ZnO	flower decorated with Fe_2O_3 rods	hydrothermal	30–40		+			+			+	
[240]	ZnO	flower decorated with Ag particles	hydrothermal	10		X			X				
[241]	ZnO	flower decorated with Au particles	hydrothermal	< 50	X	X							
[242]	ZnO	flower/aggregate	hydrothermal	20–40	+	X				X		+	
[243]	ZnO	wall	hydrothermal	10–20									
[244]	ZnO	wall	hydrothermal	10–20		X			+	X			
[245]	ZnO	wall/forest	hydrothermal	20									
[246]	ZnO	wall	hydrothermal	10–20		X							
[72]	ZnO	forest	evaporation + oxida-tion	20–30									
[247]	ZnO	forest	solvothermal	10–30	X	X				X			
[248]	ZnO	forest doped with Sn	hydrothermal	10–20						X			
[249]	ZnO	forest	hydrothermal	50									
[250]	ZnO	forest	hydrothermal	50–100		X	+				+		
[24]	ZnO	forest	solvothermal	30								+	
[251]	ZnO	rod-shaped flower with hollow core	solution	5–16	+	X	+						+
[252]	ZnO	tree	hydrothermal	30–40		X			+	X	+	+	
[4]	ZnO	film	hydrothermal	tens		X	+			+		+	
[253]	ZnO	film	solvothermal + oxi-dation	15–30					X				
[133]	ZnO	film decorated with Au particles	hydrothermal	30–60	+	+		X		+	+		
[254]	ZnO	film decorated with Pd particles	hydrothermal	15	+	+				X	+	+	
[63]	$ZnSnO_3$	forest	hydrothermal dissolution-recrystallization	15–20		X				X			

Reference	NO_2	NO	NO_x	NH_3	CO	H_2	CH_4	CO_2	O_2	H_2S	Other gases
[134]			X	+	+	+					
[135]											CH_2Cl_2, C_6H_{14}
[136]		X									
[137]				+	+						
[43]	+			+	+						ethylene glycol, benzyl alcohol
[138]	+			+							$CHCl_3$, diethyl ether
[139]				+		+					
[140]											
[141]					+	+					
[142]				+							
[143]											
[144]					X		X				
[127]					+						
[145]											
[146]											
[147]											gasoline

(*continued on next page*)

Table 4 (*continued*)

Reference	NO_2	NO	NO_x	NH_3	CO	H_2	CH_4	CO_2	O_2	H_2S	Other gases
[148]	+	+		+	+	+			+	X	N_2
[41]	X										
[149]				+	+						DMF
[150]											
[69]											
[151]		+					+			X	
[20]	X				+	+	+				
[125]	X			+						+	Cl_2, SO_2, O_3
[152]											
[51]					+	+	+				
[153]				+							
[154]				+	+	+	+		+		LPG, C_6H_{12}
[29]											
[155]	X			+	+					+	SO_2, Cl_2, O_3
[156]	X				+					+	SO_2, Cl_2, O_3
[157]											THF, CH_2Cl_2
[27]	X			+	+	+	+			+	O_3
[158]			X								
[26]	X			+							C_3H_6O
[159]			X	+	+	+					
[160]				+	+	X				+	
[161]						X					THF, ethyl acetate, 1,2-dichloroethane, DMSO, cyclohexane, acetonitrile
[47]											
[162]											
[61]				+							glycol
[77]						X[b]					
[163]											HCOOH, $CHCl_3$, CH_3CHO, C_4H_8O
[164]						X					
[165]			X								
[23]	X			+		+				+	
[40]											
[34]											
[39]											
[33]				+	+					X	$(C_2H_5)_3N$, C_6H_5Cl,
[48]	X			+		+				+	
[36]											
[126]				+							ethanoic acid, DMF
[132]	X			+		+				+	
[166]											
[167]											
[50]											
[46]											
[168]											
[21]											
[58]				+							methanamide, dimethylacetamide, DMF
[169]					+		+				
[45]				+	+						
[71]				+							C_6H_5Cl
[170]											$CHCl_3$
[171]											C_6H_{12}, 1,2-dichloroethene
[172]						+	+				

(*continued on next page*)

Table 4 (*continued*)

Reference	NO_2	NO	NO_x	NH_3	CO	H_2	CH_4	CO_2	O_2	H_2S	Other gases
[173]					+	+					
[174]	X	+		+	+						SO_2
[175]				+	+		+			+	
[176]	X										
[177]				+		+	+				H_2O
[178]	X				+						
[123]	X										
[179]											
[180]	X	+			+	+	+				SO_2
[74]	X										
[2]											
[181]				+							methanal, diethyl ether
[182]				+							
[183]				+	+	+	+				
[184]											
[22]	+			+							
[185]											
[57]					X						
[54]											
[186]				+							acetic acid, DMF
[187]				+							acetic acid, DMF
[188]											
[189]				+							DMF
[32]											acetic acid
[190]											
[191]											
[192]				+							acetic acid, DMF
[193]				+							acetic acid, DMF
[194]						+					glycol, H_2O
[195]				+	+		+	+			
[55]											
[196]				+	+						$CHCl_3$
[197]											$CHCl_3$
[3]	X										
[198]											
[199]					+						$CHCl_3$
[200]											butanone
[62]											ethyl ether, $CHCl_3$
[131]						+					glycol, H_2O
[201]											
[202]				+							
[203]											
[204]											
[205]						+		+		+	C_2H_4, C_3H_6O
[206]											butanone
[59]											
[73]			+			+					
[207]											1-butylamine, pyridine
[208]						X					
[35]											H_2O_2
[37]											
[56]	+	X		+	+		+			+	SO_2
[209]											
[210]							+				acetylene, ethane
[211]					+		+	+			gasoline

(*continued on next page*)

Table 4 (*continued*)

Reference	NO_2	NO	NO_x	NH_3	CO	H_2	CH_4	CO_2	O_2	H_2S	Other gases
[212]											
[213]											
[214]					X						
[215]	X				+	+					
[216]	X			+	+					+	Cl_2
[217]	X			+	+					+	Cl_2
[218]											
[219]											
[68]	X										
[220]										X	
[221]						X					
[222]						X					
[223]	X			+	+	+					
[78]											
[224]	X										
[225]	X										
[226]						X[c]					
[42]					+		+			+	ethene
[60]											
[49]											
[30]				+							
[227]											
[52]				+	+	+					acetic acid
[228]						+					acetic acid
[229]				+	+	+	+				CH_3NH_2, $(CH_3)_2NH$, $(CH_3)_3N$, LPG, C_5H_{12}, C_6H_{14}, C_6H_{12}, C_7H_{16}, C_9H_{20}, $C_6H_5CH_3$, $C_6H_4(CH_3)_2$, CH_2Cl_2, $CHCl_3$, CCl_4, CH_3CHO
[230]											
[64]											
[31]	+			+	+						
[231]											
[232]					+	+	+				C_5H_{12}, C_6H_{14}, C_6H_{12}, C_7H_{16}, CH_2Cl_2, $CHCl_3$, CCl_4
[53]											
[233]	X	+			+						n-hexacohol, propene
[234]					+	+	+				acetylene, CH_2Cl_2, $CHCl_3$, CCl_4
[235]				+			+				
[65]											
[66]											
[236]	+				+	+		+	+		acetylene
[236]	+				+	X		+	+		acetylene
[237]											
[238]											chlorobenzene
[124]				+	+						
[239]											$(CH_3)_3N$
[240]											
[241]											
[242]				+							gasoline
[243]	X										
[244]	+	+		+		+	+			X	H_2O, SO_2
[245]	X										
[246]											
[72]						X					

(*continued on next page*)

Table 4 (*continued*)

Reference	NO_2	NO	NO_x	NH_3	CO	H_2	CH_4	CO_2	O_2	H_2S	Other gases
[247]		+									C_6H_5Cl
[248]											
[249]											H_2O
[250]	+			+	+	+					H_2O
[24]	+			+	X	+					SO_2, Cl_2
[251]											hexamethylene
[252]				+	+						acetonitrile, C_6H_5Cl
[4]											
[253]				X							$CHCl_3$
[133]											C_6H_5Cl, acetonitrile
[254]											
[63]											

[a] Based on electrochemical sensing.
[b] Based on plasmonic sensing.
[c] Based on either chemiresistive or gasochromic sensing.

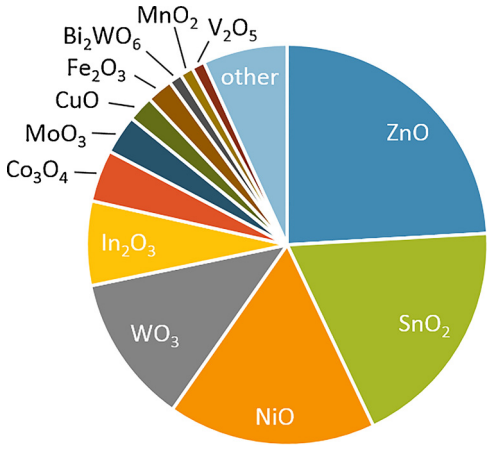

Fig. 6. Differentiation between metal oxides used for the 2D subunits in gas sensing elements (based on Table 4). For composites each individual metal oxide is counted.

concentration and mobility in a semiconductor metal oxide depend massively on crystal defects and doping levels, which suggests that the intrinsic conductance of the metal oxide matrix is of inferior importance. Alternatively, the surface of In_2O_3 may be favorable for interaction with NO_2. The particular response of In_2O_3 extends to other oxidizing gases such as O_3 [255], for which it is known that surface hydroxyl groups promote O_3 dissociation [256].

4.3.2. Acetone sensors

For acetone detection the highest responses have been reached with TiO_2, ZnO and NiO as 2D sensing materials. Maziarz et al. have reported SnO_2-decorated TiO_2 walls with an extraordinary response of 348 to 8 ppm acetone at 308 °C [73]. Though the SnO_2 surface was believed to be the primary sensing surface, TiO_2 donates electrons to increase oxygen ionosorption on SnO_2 and offers rapid electron transport [73,257,258]. Non-decorated TiO_2 walls yielded a response of about 2 towards an acetone concentration of 2 ppm. Xie et al. have reported ZnO flower architectures that reached a response of 362 to 100 ppm acetone at 300 °C and could detect concentrations down to 1 ppm [227]. The response towards acetone was about 12 times larger than the response towards ethanol. Lu et al. have reported the use of 2D NiO nanoflakes to decorate 1D nanorod-assembled flowers of ZnO [126]. The local *p-n* junctions between NiO (p-type) and ZnO (n-type) increase the electron depletion and thus the electrical resistivity in ZnO. A response of 205 for 100 ppm acetone was reached at 240 °C and concentrations were detected down to 10 ppm. The response towards acetone was 2 times larger than that towards ethanol and 4–15 times larger than that towards ethanoic acid, methanol, DMF and NH_3. Wang et al. have reported W-doped NiO flowers with a similar response of 198 for 100 ppm acetone at 250 °C, though the response towards acetone was only about 1.2 times larger than that towards ethanol [45]. Doping with W decreases the hole concentration and thus the conductivity in NiO. Also, an increasing specific surface area was observed as compared to undoped NiO flowers.

4.3.3. Ethanol sensors

For ethanol detection many different materials and sensor designs have been reported. The highest responses were reached with ZnO sensors and with a composite of CoO, SnO and SnO_2. Responses to 100 ppm ethanol of about 340 and 285 have been reported for ZnO flower architectures, respectively, at 370 °C by Xie et al. [227] and at 400 °C by Zhang et al. [232]. In both cases the gas diffusion inside the 3D assembly was facilitated by mesopores in the 2D ZnO nanoflakes and successful detection was demonstrated down to 0.1–1 ppm. Guo has reported a ZnO flower architecture with similarly high performance at low ethanol concentrations, i.e. responses of respectively 17 and 112

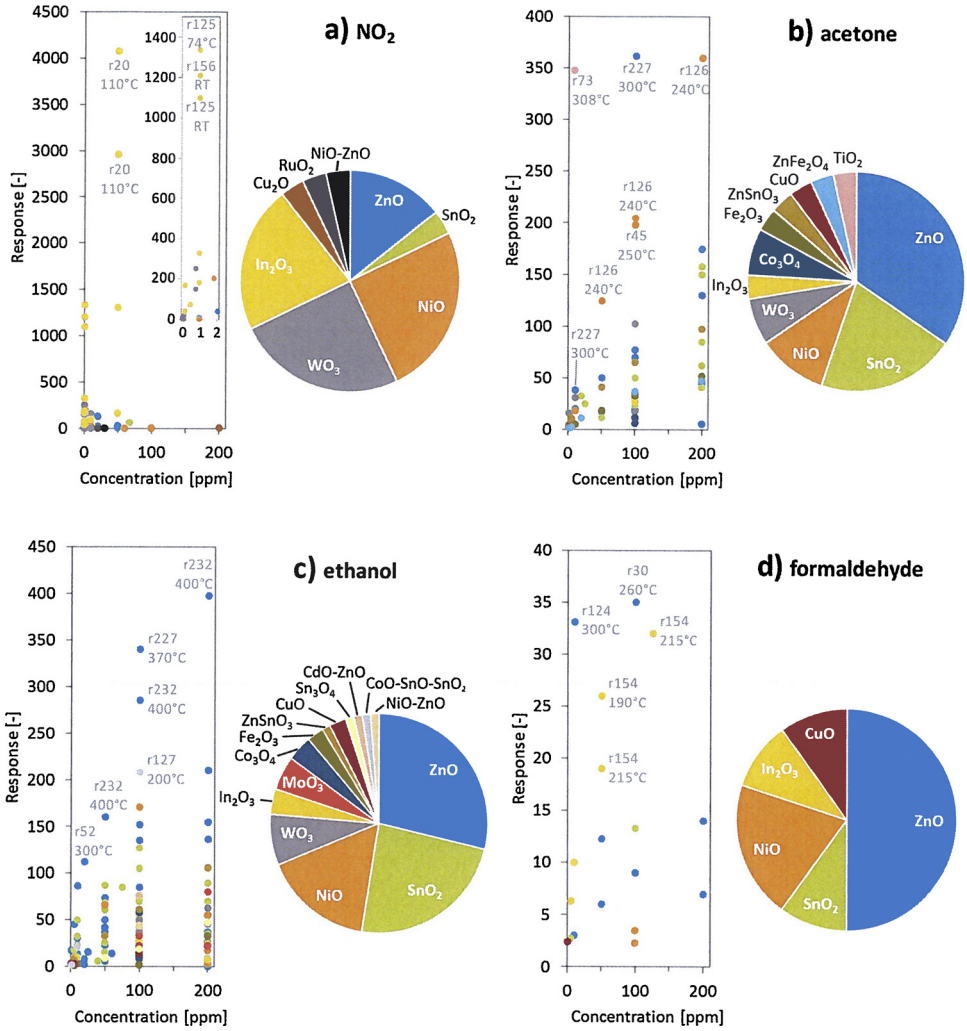

Fig. 7. Overview of reported maximum responses and used materials (based on the number of publications) for 2D metal oxide gas sensors for (a) NO_2 detection with the inset zooming in on low concentrations, (b) acetone detection, (c) ethanol detection and (d) formaldehyde detection. All sensors from Table 4 with selective behavior towards NO_2, acetone, ethanol and/or formaldehyde are included except [39,69,135,147,185,199].

for 1 and 20 ppm at 300 °C, but for higher concentrations its response leveled off at about 130 [52]. Wang et al. have reported a flower architecture of a composite of CoO, SnO and SnO_2 [127]. The many *p-n* junctions between CoO (p-type) and SnO_2 (n-type) yield depletion of charge carriers and thus an increasing resistance in the sensing body. Also, CoO was believed to catalyze the dissociation of ethanol molecules on the sensor surface. A Co:Sn ratio of 1 yielded a response of 208 to 100 ppm ethanol, which is lower than the responses of ZnO flowers mentioned above, but an important advantage of the Co/Sn oxide sensor is its significantly lower sensing temperature of 200 °C. Room-temperature ethanol sensing has been reported by Alenezi et al. using ZnO nanodisks that were activated with UV irradiation [4]. Though UV irradiation decreases the overall amount of oxygen adsorbed on the sensor surface, the presence of excitons promotes oxygen adsorption in the more active atomic form (O^-) rather than the less active molecular form (O_2^-). A response of about 1.3 was reached for 200 ppm ethanol under 1.6 mW cm^{-2} UV irradiation.

4.3.4. Formaldehyde sensors

Formaldehyde detection has been reported with the highest responses for ZnO and In_2O_3 sensors. Cao et al. reached a response of 35 for 100 ppm formaldehyde at 260 °C with a ZnO flower architecture [30]. The response towards formaldehyde was 2.3 times larger than the response towards ethanol, 4 times larger than the response towards acetone and > 10 times larger than the response towards NH_3, toluene and benzene. ZnO flowers with Fe doping have been reported by Guo, yielding a response of 33 for a formaldehyde concentration of only 10 ppm at 300 °C [124]. Substituting Zn^{2+} in the ZnO lattice with Fe^{3+} causes the release of more electrons in the conduction band. This facilitates the reduction of O_2 at the sensor surface and thereby increases the number of sites where formaldehyde can be oxidized. Also, Fe doping is believed to enhance gas sensing via increasing the oxygen vacancy concentration. Zhang et al. have reported In_2O_3 flowers with mesoporous petals that detected 50 ppm formaldehyde at 190 °C with a response of 26 [154]. At 215 °C the responses were 19 for 50 ppm and 32 for 125 ppm.

4.3.5. Comparison

When considering the performance of various metal oxides with respect to the number of literature reports (see Fig. 3), In_2O_3 has yielded several of the sensors with the highest responses while it represents only 7% of the gas sensor reports included in this review. In terms of sensitivity (note that speed and stability of the sensors are not considered in the present review) In_2O_3 thus appears promising for further development in 2D-based sensing elements, though the precise reason for its success remains unclear (see Section 4.3.1). ZnO has been used for many of the most responding as well as least responding gas sensors, indicating no intrinsic superiority of ZnO as compared to the other metal oxides. As for SnO_2, it has been used in about 20% of the literature reports on gas sensors included in this review and has been

Table 5
Details of 2D metal oxide sensors with the highest responses for various target gases.

Target species	Concentration [ppm]	Response	Temperature [°C]	2D metal oxide	Reference
methanol	1/5	2.7/8.4	230	NiO (flower)	[21]
methanol	20/100	30/108	255	NiO (flower, porous petals, Fe_2O_3-decorated)	[58]
butanol	2/100	31/161	300	WO_3 (film)	[78]
toluene	5	305	250	Co_3O_4 (hollow flower, Pd-decorated)	[139]
xylene	5	361	250	Co_3O_4 (hollow flower, Pd-decorated)	[139]
xylene	5	164	250	Co_3O_4 (hollow flower)	[139]
chlorobenzene	100	6.9	200	ZnO (flower, porous petals)	[238]
acetic acid	50/100/200	15/132/351	340	SnO_2 (flower, porous petals)	[32]
acetylene	1/200/1/200	10/164/4/22	400/400/285/285	ZnO (aggregated film, porous flakes)	[234]
acetylene	100	12.3	200	ZnO (flower, Ag- and RGO-decorated)	[236]
dimethylamine	1/200	16.8/2087	370	ZnO (flower, porous petals, rod-decorated)	[229]
trimethylamine	20/200	3.9/11.6	260	ZnO (flower, Fe_2O_3-decorated)	[239]
glycol	5/100	5/90	240	SnO_2 (flower, Zn-doped)	[194]
CO	10/40	> 25/ > 100	RT	Co_3O_4 (aggregated film, porous flakes)	[144]
CH_4	10/40	> 25/ > 100	RT	Co_3O_4 (aggregated film, porous flakes)	[144]
H_2	100	15	200	ZnO (flower)	[236]
H_2	100	3.3/11.4/20.5	25/100/300	MnO_2 (forest, Pd-decorated)	[160]
H_2S	2.5/50	164/2185	200	ZnO (wall, porous)	[244]
H_2O	50%/90% RH	9/345	25	ZnO (wall, porous)	[244]
H_2O	60	2	RT	ZnO (forest)	[249]
NH_3	50/200	4.3/8.4	250	ZnO (film, porous)	[253]
NO_x	0.1/1/10	2/65/213	120	In_2O_3 (forest, porous)	[158]
NO	20	203[a]	200	WO_3 (flower, porous rough petals)	[56]

[a] For an oxygen-free reference atmosphere.

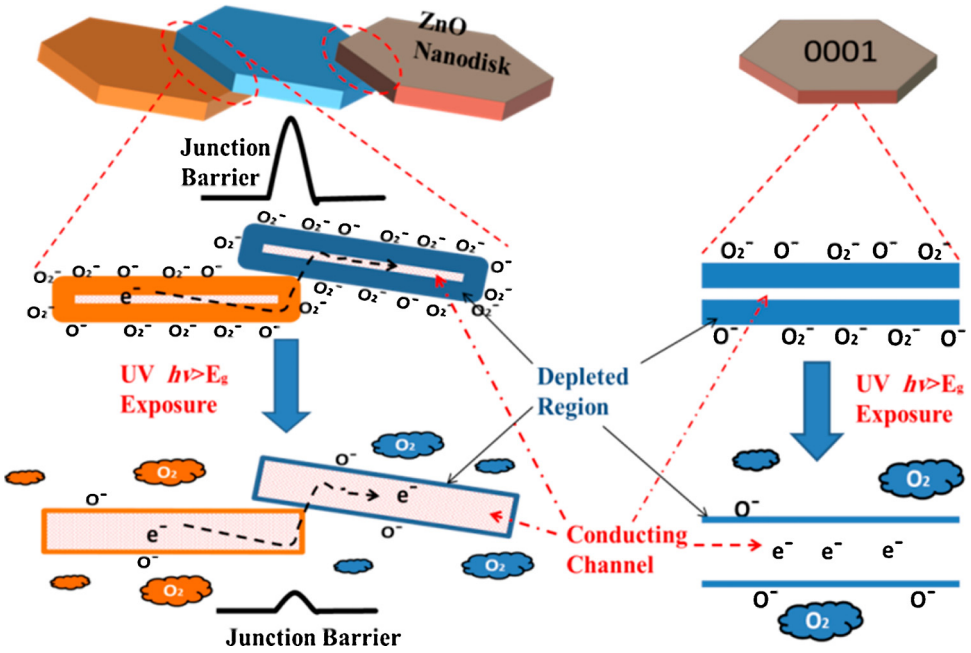

Fig. 8. Schematic representation of the photoelectric sensing mechanism in a stack of ZnO nanodisks and in a single nanodisk. Reprinted with permission from [19]. Copyright 2014 American Chemical Society.

used for the detection of many different target gases, but is almost always outperformed by other metal oxides in terms of response. For selective detection of acetic acid and glycol only SnO_2-based 2D sensors were found.

As for the relation between 2D nanoflake thickness and sensor response, in principle, thinner nanoflakes yield more surface area and thus more active sensing sites per unit volume of metal oxide. However, the used amount of metal oxide is often not of critical importance in sensor design. The active surface area of a sensor can then also be tuned by e.g. changing the dimensions and architecture of the substrate and the packing density of the metal oxide nanoflakes. Since reports on sensor performance generally do not consider the amount of metal oxide used in a sensor, care must be taken in interpreting correlations between response and nanoflake dimensions or specific surface areas. The various best-performing sensors discussed above have nanoflake thicknesses over the entire size range up to 50 nm (the limit of this review), not indicating a general design rule for sensor optimization.

In addition to the metal oxide loading on a specific device, other fabrication and operation aspects can also significantly influence the sensor performance. The electrical contact depends on the bonding between the sensing material and the device and it may thus be advantageous to grow 2D-based architectures directly onto the sensing device. However, morphological evolution during subsequent processing of the sensor can also be detrimental [259]. As for operation

conditions, sensor responses and selectivities vary with e.g. the gas flow rate [260], the environmental humidity [122] and the operation temperature. Combined signals may be deconvoluted by applying temperature profiles to a single sensor [261] or by using so-called electronic noses, i.e. arrays of different sensors of which the responses are processed with pattern recognition software [262]. Resistive switching, i.e. tuning the metal oxide resistivity by applying a voltage bias, can also be used to increase selectivities and deconvolute combined signals [263].

5. 2D nanoflakes for radiation sensing

Few examples have been reported of 2D nanoflake sensors for detection of radiation. Alenezi et al. have reported on UV sensing with 2D ZnO nanodisks of 10–100 nm thickness, employing a photoelectric sensing mechanism [19]. UV irradiation generates electron-hole pairs in the metal oxide lattice. The holes migrate to the surface and are neutralized by adsorbed oxygen ions, while the electrons increase the conductivity in the metal oxide phase. Sensing was demonstrated with both individual and stacked ZnO nanodisks and the conceptual difference between both cases is schematically indicated in Fig. 8 [19]. Here the junction barriers change because of UV-induced fluctuations in the ionosorbed oxygen population, but the same principle holds for fluctuations of ionosorbed species induced by reactive gases as discussed in Section 4. The tunnel current across the junction barriers between stacked nanodisks is exponentially related to the barrier height and thus highly sensitive to small changes. The sensor response was about 1000 for a single nanodisk and about 1500 for a stack of nanodisks. The single-nanodisk detector showed a photoresponsivity of 3386 A W^{-1} at 3 V. Hoa et al. have prepared a photoresistive sensor with tree-like structures of 1D ZnO nanorods decorated with 10–20 nm thick 2D NiO nanoflakes and thus containing many *p-n* junctions [44]. The response reached over 400% after UV exposure for about 2 min and still increased significantly, yielding a response improvement of 1–2 orders of magnitude as compared to both metal oxides separately. Uthirakumar et al. have increased the UV sensing performance of polymethylmethacrylate films by incorporating 0.2% CuO nanoflakes, resulting in a more than threefold increase of UV absorption capability [264].

6. Perspective

In the field of gas sensors, the concept of using 2D metal oxides is well established. Proof-of-principle sensor devices have been prepared with many different materials via easy and scalable routes and several studies have demonstrated competitive performances. However, further device optimization is needed to enable widespread application in industry and day-to-day life. The geometrical benefits of 2D nanoflakes can be exploited best when they are assembled in 3D hierarchical architectures with moderate packing density to ensure extensive surface exposure. Achieving high selectivities is a difficult challenge with the intrinsically unselective chemiresistive sensing mechanism, but various routes can be explored in addition to the widely investigated approach of chemical sensitization (adding catalysts). For example, illumination of metal oxide sensing elements either above or below their band gap has been proposed to facilitate (selective) desorption of surface species [116]. This increases reversibility and selectivity at relatively low operation temperatures. An alternative approach is to integrate the sensor with a permselective membrane. Kato et al. have reported the use of cross-linked polysiloxane monolayers on top of sensor electrodes to detect NO in solution while preventing interfering species such as nitrite, dopamine, adrenalin and uric acid from reaching the electrode surface [265,266]. Recently, incorporation of zeolites as both filtering and catalytic component has been investigated extensively because it enables discrimination based on molecular size, shape and affinity [117,267]. Membrane layers with somewhat larger pores can induce discrimination based on molecular weight (exploit Knudsen diffusion) [117]. Finally, exploiting particular surface energy landscapes via crystal facet engineering is a promising road towards higher and fine-tuned sensor selectivities. Though facet engineering has been applied in several cases to promote specific chemical interactions, it is not yet generally adopted as point of consideration.

Solute sensing with 2D metal oxides is still relatively new, but pioneering reports already set the bar in minimizing the detection limit. Sensing in solution is particularly suitable for exploiting mono- or few-layer nanosheets that do not have the rigidity to form and maintain hierarchical assemblies under dry conditions. Keeping these ultrathin crystallites in suspension yields a relatively robust and easy-to-handle system that provides full surface exposure of the nanosheets. Mono- or few-layer crystallites generally provide unsurpassed structural and chemical surface homogeneity, which is favorable for achieving well-defined sensor responses. Also, new sensing strategies may be developed based on quantum confinement effects in ultrathin nanosheets. As for plasmonic sensing, this generally varies with the shape and size of nanoparticles [268] and thus performances may be improved by controlling the size of 2D nanoflakes. A new and still unexplored strategy to modulate the selectivity of 2D sensing elements further is to introduce specific adsorption sites using controlled ion doping strategies. Doping with aliovalent dopants will affect both the nanosheet conductivity and may introduce (redox-active) surface sites for molecular or ionic recognition.

References

[1] H. Wang, A.L. Rogach, Hierarchical SnO2 nanostructures: recent advances in design, synthesis, and applications, Chem. Mater. 26 (2014) 123–133.
[2] T. Li, W. Zeng, H. Long, Z. Wang, Nanosheet-assembled hierarchical SnO2 nanostructures for efficient gas-sensing applications, Sens. Actuators B Chem. 231 (2016) 120–128.
[3] H. Wang, K. Dou, W.Y. Teoh, Y. Zhan, T.F. Hung, F. Zhang, J. Xu, R. Zhang, A.L. Rogach, Engineering of facets band structure, and gas-sensing properties of hierarchical Sn2+-doped SnO2 nanostructures, Adv. Funct. Mater. 23 (2013) 4847–4853.
[4] M.R. Alenezi, A.S. Alshammari, K.D.G.I. Jayawardena, M.J. Beliatis, S.J. Henley, S.R.P. Silva, Role of the exposed polar facets in the performance of thermally and UV activated ZnO nanostructured gas sensors, J. Phys. Chem. C. 117 (2013) 17850–17858.
[5] N. Sakai, Y. Ebina, K. Takada, T. Sasaki, Electronic band structure of titania semiconductor nanosheets revealed by electrochemical and photoelectrochemical studies, J. Am. Chem. Soc. 126 (2004) 5851–5858.
[6] Y. Omomo, T. Sasaki, L. Wang, M. Watanabe, Redoxable nanosheet crystallites of MnO2 derived via delamination of a layered manganese oxide, J. Am. Chem. Soc. 125 (2003) 3568–3575.
[7] R. Zhang, W. Chen, Recent advances in graphene-based nanomaterials for fabricating electrochemical hydrogen peroxide sensors, Biosens. Bioelectron. 89 (2017) 249–268.
[8] X. Bo, M. Zhou, L. Guo, Electrochemical sensors and biosensors based on less aggregated graphene, Biosens. Bioelectron. 89 (2017) 167–186.
[9] S. Campuzano, M. Pedrero, G.-P. Nikoleli, J.M. Pingarrón, D.P. Nikolelis, Hybrid 2D-nanomaterials-based electrochemical immunosensing strategies for clinical biomarkers determination, Biosens. Bioelectron. 89 (2017) 269–279.
[10] T. Zhang, J. Liu, C. Wang, X. Leng, Y. Xiao, L. Fu, Synthesis of graphene and related two-dimensional materials for bioelectronics devices, Biosens. Bioelectron. 89 (2017) 28–42.
[11] W. Fu, L. Jiang, E.P. van Geest, L.M.C. Lima, G.F. Schneider, Sensing at the surface of graphene field-effect transistors, Adv. Mater. 29 (2017) 1603610.
[12] J. Xu, Y. Wang, S. Hu, Nanocomposites of graphene and graphene oxides: synthesis, molecular functionalization and application in electrochemical sensors and biosensors. A review, Microchim. Acta 184 (2017) 1–44.
[13] L. Wang, Q. Xiong, F. Xiao, H. Duan, 2D nanomaterials based electrochemical biosensors for cancer diagnosis, Biosens. Bioelectron. 89 (2017) 136–151.
[14] P. Bollella, G. Fusco, C. Tortolini, G. Sanzò, G. Favero, L. Gorton, R. Antiochia, Beyond graphene: electrochemical sensors and biosensors for biomarkers detection, Biosens. Bioelectron. 89 (2017) 152–166.
[15] J. Ping, Z. Fan, M. Sindoro, Y. Ying, H. Zhang, Recent advances in sensing applications of two-dimensional transition metal dichalcogenide nanosheets and their composites, Adv. Funct. Mater. 27 (2017) 1605817.
[16] S. Yang, C. Jiang, S. Wei, Gas sensing in 2D materials, Appl. Phys. Rev. 4 (2017) 21304.
[17] X. Liu, T. Ma, N. Pinna, J. Zhang, Two-dimensional nanostructured materials for gas sensing, Adv. Funct. Mater. 27 (2017) 1702168.
[18] Y. Shu, J. Xu, J. Chen, Q. Xu, X. Xiao, D. Jin, H. Pang, X. Hu, Ultrasensitive electrochemical detection of H2O2 in living cells based on ultrathin MnO2

nanosheets, Sens. Actuators B Chem. 252 (2017) 72–78.
[19] M.R. Alenezi, A.S. Alshammari, T.H. Alzanki, P. Jarowski, S.J. Henley, S.R.P. Silva, ZnO nanodisk based UV detectors with printed electrodes, Langmuir 30 (2014) 3913–3921.
[20] J. Hu, Y. Liang, Y. Sun, Z. Zhao, M. Zhang, P. Li, W. Zhang, Y. Chen, S. Zhuiykov, Highly sensitive NO2 detection on ppb level by devices based on Pd-loaded In2O3 hierarchical microstructures, Sen. Actuators B Chem. 252 (2017) 116–126.
[21] Y. Zhang, L. Xie, C. Yuan, C. Zhang, S. Liu, Y. Peng, H. Li, M. Zhang, Preparation of 3D rose-like nickel oxide nanoparticles by electrodeposition method and application in gas sensors, J. Mater. Sci. Mater. Electron. 27 (2016) 1817–1827.
[22] H. Yu, T. Yang, Z. Wang, Z. Li, B. Xiao, Q. Zhao, M. Zhang, Facile synthesis cedar-like SnO2 hierarchical micro-nanostructures with improved formaldehyde gas sensing characteristics, J. Alloys Compd. 724 (2017) 121–129.
[23] L.T. Hoa, H.N. Tien, V.H. Luan, J.S. Chung, S.H. Hur, Fabrication of a novel 2D-graphene/2D-NiO nanosheet-based hybrid nanostructure and its use in highly sensitive NO2 sensors, Sens. Actuators B Chem. 185 (2013) 701–705.
[24] Y. Zeng, L. Qiao, Y. Bing, M. Wen, B. Zou, W. Zheng, T. Zhang, G. Zou, Development of microstructure CO sensor based on hierarchically porous ZnO nanosheet thin films, Sens. Actuators B Chem. 173 (2012) 897–902.
[25] Z. Cui, H. Yin, Q. Nie, Controllable preparation of hierarchically core-shell structure NiO/C microspheres for non-enzymatic glucose sensor, J. Alloys Compd. 632 (2015) 402–407.
[26] L. Gao, Z. Cheng, Q. Xiang, Y. Zhang, J. Xu, Porous corundum-type In2O3 nanosheets: synthesis and NO2 sensing properties, Sen. Actuators B Chem. 208 (2015) 436–443.
[27] X. Xu, P. Zhao, D. Wang, P. Sun, L. You, Y. Sun, X. Liang, F. Liu, H. Chen, G. Lu, Preparation and gas sensing properties of hierarchical flower-like In2O3 microspheres, Sens. Actuators B Chem. 176 (2013) 405–412.
[28] Y. Zhao, J. Zhao, Y. Li, D. Ma, S. Hou, L. Li, X. Hao, Z. Wang, Room temperature synthesis of 2D CuO nanoleaves in aqueous solution, Nanotechnology 22 (2011) 115604.
[29] J. Liu, T. Luo, F. Meng, K. Qian, Y. Wan, J. Liu, Porous hierarchical In2O3 micro-/nanostructures: preparation, formation mechanism, and their application in gas sensors for noxious volatile organic compound detection, J. Phys. Chem. C. 114 (2010) 4887–4894.
[30] J. Cao, S. Wang, H. Zhang, Controllable synthesis of zinc oxide hierarchical architectures and their excellent formaldehyde gas sensing performances, Mater. Lett. 202 (2017) 44–47.
[31] J. Cui, J. Sun, X. Liu, J. Li, X. Ma, T. Chen, Fabrication of hierarchical flower-like porous ZnO nanostructures from layered ZnC2O4. 3Zn(OH)2 and gas sensing properties, Appl. Surf. Sci. 308 (2014) 17–23.
[32] T.T. Wang, S.Y. Ma, L. Cheng, X.L. Xu, J. Luo, X.H. Jiang, W.Q. Li, W.X. Jin, X.X. Sun, Performance of 3D SnO2 microstructure with porous nanosheets for acetic acid sensing, Mater. Lett. 142 (2015) 141–144.
[33] T. Yu, X. Cheng, X. Zhang, L. Sui, Y. Xu, S. Gao, H. Zhao, L. Huo, Highly sensitive H2S detection sensors at low temperature based on hierarchically structured NiO porous nanowall arrays, J. Mater. Chem. A. 3 (2015) 11991–11999.
[34] X. San, G. Zhao, G. Wang, Y. Shen, D. Meng, Y. Zhang, F. Meng, Assembly of 3D flower-like NiO hierarchical architectures by 2D nanosheets: synthesis and their sensing properties to formaldehyde, RSC Adv. 7 (2017) 3540–3549.
[35] H. Pang, Y. Dong, S.L. Ting, J. Lu, C.M. Li, D.-H. Kim, P. Chen, 2D single- or double-layered vanadium oxide nanosheet assembled 3D microflowers: controlled synthesis, growth mechanism, and applications, Nanoscale 5 (2013) 7790–7794.
[36] X. San, G. Wang, B. Liang, J. Ma, D. Meng, Y. Shen, Flower-like NiO hierarchical microspheres self-assembled with nanosheets: surfactant-free solvothermal synthesis and their gas sensing properties, J. Alloys Compd. 636 (2015) 357–362.
[37] J. Huang, X. Xu, C. Gu, M. Yang, M. Yang, J. Liu, Large-scale synthesis of hydrated tungsten oxide 3D architectures by a simple chemical solution route and their gas-sensing properties, J. Mater. Chem. 21 (2011) 13283–13289.
[38] D. He, X. He, K. Wang, X. Yang, X. Yang, X. Li, Z. Zou, Nanometer-sized manganese oxide-quenched fluorescent oligonucleotides: an effective sensing platform for probing biomolecular interactions, Chem. Commun. 50 (2014) 11049–11052.
[39] L. Lin, T. Liu, W. Yu, Z. Gou, W. Zeng, Synthesis of multifarious hierarchical flower-like NiO and their gas-sensing properties, Mater. Res. Bull. 48 (2013) 2730–2736.
[40] J. Wang, W. Zeng, Z. Wang, Assembly of 2D nanosheets into 3D flower-like NiO: Synthesis and the influence of petal thickness on gas-sensing properties, Ceram. Int. 42 (2016) 4567–4573.
[41] S. Cao, H. Chen, T. Han, C. Zhao, L. Peng, Rose-like Cu2O nanoflowers via hydrothermal synthesis and their gas sensing properties, Mater. Lett. 180 (2016) 135–139.
[42] X. Zhou, X. Li, H. Sun, P. Sun, X. Liang, F. Liu, X. Hu, G. Lu, Nanosheet-assembled ZnFe2O4 hollow microspheres for high-sensitive acetone sensor, ACS Appl. Mater. Interfaces. 7 (2015) 15414–15421.
[43] L. Li, C. Zhang, R. Zhang, X. Gao, S. He, M. Liu, X. Li, W. Chen, 2D ultrathin Co3O4 nanosheet array deposited on 3D carbon foam for enhanced ethanol gas sensing application, Sens. Actuators B Chem. 244 (2017) 664–672.
[44] L.T. Hoa, H.N. Tien, S.H. Hur, A highly sensitive UV sensor composed of 2D NiO nanosheets and 1D ZnO nanorods fabricated by a hydrothermal process, Sens. Actuators A Phys. 207 (2014) 20–24.
[45] C. Wang, J. Liu, Q. Yang, P. Sun, Y. Gao, F. Liu, J. Zheng, G. Lu, Ultrasensitive and low detection limit of acetone gas sensor based on W-doped NiO hierarchical nanostructure, Sens. Actuators B Chem. 220 (2015) 59–67.
[46] Q. Gao, W. Zeng, R. Miao, Synthesis of multifarious hierarchical flower-like NiO and their gas-sensing properties, J. Mater. Sci. Mater. Electron. 27 (2016) 9410–9416.
[47] Y. Li, Morphology-controllable synthesis of three-dimensional a-MoO3 and their applications in gas sensing, Phys. E 94 (2017) 22–24.
[48] Y.-L.T. Ngo, S.H. Hur, Low-temperature NO2 gas sensor fabricated with NiO and reduced graphene oxide hybrid structure, Mater. Res. Bull. 84 (2016) 168–176.
[49] F. Meng, S. Ge, Y. Jia, B. Sun, Y. Sun, C. Wang, H. Wu, Z. Jin, M. Li, Interlaced nanoflake-assembled flower-like hierarchical ZnO microspheres prepared by bi-solvents and their sensing properties to ethanol, J. Alloys Compd. 632 (2015) 645–650.
[50] R. Miao, W. Zeng, Q. Gao, SDS-assisted hydrothermal synthesis of NiO flake-flower architectures with enhanced gas-sensing properties, Appl. Surf. Sci. 384 (2016) 304–310.
[51] J. Hu, X. Wang, M. Zhang, Y. Sun, P. Li, W. Zhang, K. Lian, L. Chen, Y. Chen, Synthesis and characterization of flower-like MoO3/In2O3 microstructures for highly sensitive ethanol detection, RSC Adv. 7 (2017) 23478–23485.
[52] W. Guo, ZnO nanosheets assembled different hierarchical structures and their gas sensing properties, J. Mater. Sci. Mater. Electron. 27 (2016) 7302–7310.
[53] W. Guo, T. Liu, W. Zeng, D. Liu, Y. Chen, Z. Wang, Gas-sensing property improvement of ZnO by hierarchical flower-like architectures, Mater. Lett. 65 (2011) 3384–3387.
[54] Q. Zhou, W. Chen, J. Li, C. Tang, H. Zhang, Nanosheet-assembled flower-like SnO2 hierarchical structures with enhanced gas-sensing performance, Mater. Lett. 161 (2015) 499–502.
[55] W. Zeng, H. Zhang, Y. Li, W. Chen, Z. Wang, Hydrothermal synthesis of hierarchical flower-like SnO2 nanostructures with enhanced ethanol gas sensing properties, Mater. Res. Bull. 57 (2014) 91–96.
[56] Z.-X. Cai, H.-Y. Li, J.-C. Ding, X. Guo, Hierarchical flowerlike WO3 nanostructures assembled by porous nanoflakes for enhanced NO gas sensing, Sens. Actuators B Chem. 246 (2017) 225–234.
[57] Q. Wang, C. Wang, H. Sun, P. Sun, Y. Wang, J. Lin, G. Lu, Microwave assisted synthesis of hierarchical Pd/SnO2 nanostructures for CO gas sensor, Sens. Actuators B Chem. 222 (2016) 257–263.
[58] W. Tan, J. Tan, L. Fan, Z. Yu, J. Qian, X. Huang, Fe2O3-loaded NiO nanosheets for fast response/recovery and high response gas sensor, Sens. Actuators B Chem. 256 (2018) 282–293.
[59] X. Li, F. Wang, J. Tu, H.U. Shah, J. Hu, Y. Li, Y. Lu, M. Xu, Synthesis and ethanol sensing properties of novel hierarchical Sn3O4 nanoflowers, J. Nanomater. 2015 (2015) 980170.
[60] X. Qu, M. Wang, W. Sun, R. Yang, Hierarchical flower-like ZnO microstructures: preparation, formation mechanism and application in gas sensor, J. Mater. Sci. Mater. Electron. (2017), http://dx.doi.org/10.1007/s10854-017-7338-z.
[61] H. Yan, P. Song, S. Zhang, Z. Yang, Q. Wang, Facile fabrication and enhanced gas sensing properties of hierarchical MoO3 nanostructures, RSC Adv. 5 (2015) 72728–72735.
[62] J. Liu, F. Meng, Y. Zhong, J. Liu, G. Chen, Y. Wan, K. Qian, S. Mouli, Assembly formation mechanism, and enhanced gas-sensing properties of porous and hierarchical SnO2 hollow nanostructures, J. Mater. Res. 25 (2010) 1992–2000.
[63] Y. Chen, L. Yu, Q. Li, Y. Wu, Q. Li, T. Wang, An evolution from 3D face-centered-cubic ZnSnO3 nanocubes to 2D orthorhombic ZnSnO3 nanosheets with excellent gas sensing performance, Nanotechnology 23 (2012) 415501.
[64] M. Yin, S. Liu, Controlled ZnO hierarchical structure for improved gas sensing performance, Sens. Actuators B Chem. 209 (2015) 343–351.
[65] S. Wang, Z. Li, P. Wang, C. Xiao, R. Zhao, B. Xiao, T. Yang, M. Zhang, Facile synthesis and enhanced gas sensing properties of In2O3 nanoparticle-decorated ZnO hierarchical architectures, CrystEngComm 16 (2014) 5716–5723.
[66] S. Wang, P. Wang, Z. Li, C. Xiao, B. Xiao, R. Zhao, T. Yang, M. Zhang, Highly enhanced methanol gas sensing properties by Pd0.5Pd3O4 nanoparticle loaded ZnO hierarchical structures, RSC Adv. 4 (2014) 35375–35382.
[67] W. Zhai, C. Wang, P. Yu, Y. Wang, L. Mao, Single-layer MnO2 nanosheets suppressed fluorescence of 7-hydroxycoumarin: mechanistic study and application for sensitive sensing of ascorbic acid in vivo, Anal. Chem. 86 (2014) 12206–12213.
[68] S. Bai, K. Zhang, R. Luo, D. Li, A. Chen, C.-C. Liu, Sonochemical synthesis of hierarchically assembled tungsten oxides with excellent NO2-sensing properties, Mater. Lett. 111 (2013) 32–34.
[69] X. Shen, Q. Liu, Z. Ji, G. Zhu, H. Zhou, K. Chen, Controlled synthesis and gas sensing properties of porous Fe2O3/NiO hierarchical nanostructures, CrystEngComm 17 (2015) 5522–5529.
[70] M. Hu, Y. Yamauchi, Synthesis of a titanium-containing Prussian-blue analogue with a well-defined cube structure and its thermal conversion into a nanoporous titanium-iron-based oxide, Chem. – An Asian J. 6 (2011) 2282–2286.
[71] C. Yuan, H. Li, L. Xie, F. Wang, H. Deng, F. Chang, Y. Sun, Flower-like NiO nanostructures synthesized by electrodeposition method for efficient detection of toluene gas, RSC Adv. 5 (2015) 92128–92133.
[72] M. Tonezzer, S. Iannotta, H2 sensing properties of two-dimensional zinc oxide nanostructures, Talanta 122 (2014) 201–208.
[73] W. Maziarz, A. Kusior, A. Trenczek-Zajac, Nanostructured TiO2-based gas sensors with enhanced sensitivity to reducing gases, Beilstein J. Nanotechnol. 7 (2016) 1718–1726.
[74] S.-J. Choi, J.-S. Jang, H.J. Park, I.-D. Kim, Optically sintered 2D RuO2 nanosheets: temperature-controlled NO2 reaction, Adv. Funct. Mater. 27 (2017) 1606026.
[75] M.M.Y.A. Alsaif, K. Latham, M.R. Field, D.D. Yao, N.V. Medhekar, G.A. Beane, R.B. Kaner, S.P. Russo, J.Z. Ou, K. Kalantar-zadeh, Tunable plasmon resonances in two-dimensional molybdenum oxide nanoflakes, Adv. Mater. 26 (2014) 3931–3937.
[76] M.M.Y.A. Alsaif, M.R. Field, T. Daeneke, A.F. Chrimes, W. Zhang, B.J. Carey, K.J. Berean, S. Walia, J. Van Embden, B. Zhang, K. Latham, K. Kalantar-zadeh, J.Z. Ou, Exfoliation solvent dependent plasmon resonances in two-dimensional

sub-stoichiometric molybdenum oxide nanoflakes, ACS Appl. Mater. Interfaces. 8 (2016) 3482–3493.
[77] M.M.Y.A. Alsaif, M.R. Field, B.J. Murdoch, T. Daeneke, K. Latham, A.F. Chrimes, A.S. Zoolfakar, S.P. Russo, J.Z. Ou, K. Kalantar-zadeh, Substoichiometric two-dimensional molybdenum oxide flakes: a plasmonic gas sensing platform, Nanoscale 6 (2014) 12780–12791.
[78] D. Chen, X. Hou, H. Wen, Y. Wang, H. Wang, X. Li, R. Zhang, H. Lu, H. Xu, S. Guan, J. Sun, L. Gao, The enhanced alcohol-sensing response of ultrathin WO3 nanoplates, Nanotechnology 21 (2010) 35501.
[79] H. Yuan, D. Dubbink, R. Besselink, J.E. Ten Elshof, The rapid exfoliation and subsequent restacking of layered titanates driven by an acid-base reaction, Angew. Chemie – Int. Ed. 54 (2015) 9239–9243.
[80] G. Blatter, F. Greuter, Carrier transport through grain boundaries in semiconductors, Phys. Rev. B. 33 (1986) 3952–3966.
[81] E. Comini, Metal oxide nano-crystals for gas sensing, Anal. Chim. Acta 568 (2006) 28–40.
[82] G. Korotcenkov, The role of morphology and crystallographic structure of metal oxides in response of conductometric-type gas sensors, Mater. Sci. Eng. R 61 (2008) 1–39.
[83] Y. Yuan, S. Wu, F. Shu, Z. Liu, An MnO2 nanosheet as a label-free nanoplatform for homogeneous biosensing, Chem. Commun. 50 (2014) 1095–1097.
[84] N. Dhenadhayalan, K. Yadav, M.I. Sriram, H.-L. Lee, K.-C. Lin, Ultra-sensitive DNA sensing of a prostate-specific antigen based on 2D nanosheets in live cells, Nanoscale 9 (2017) 12087–12095.
[85] S. Lin, H. Cheng, Q. Ouyang, H. Wei, Deciphering the quenching mechanism of 2D MnO2 nanosheets towards Au nanocluster fluorescence to design effective glutathione biosensors, Anal. Methods 8 (2016) 3935–3940.
[86] S. Balendhran, S. Walia, M. Alsaif, E.P. Nguyen, J.Z. Ou, S. Zhuiykov, S. Sriram, M. Bhaskaran, K. Kalantar-zadeh, Field effect biosensing platform based on 2D a-MoO3, ACS Nano 7 (2013) 9753–9760.
[87] L.-C. Jiang, W.-D. Zhang, A highly sensitive nonenzymatic glucose sensor based on CuO nanoparticles-modified carbon nanotube electrode, Biosens. Bioelectron. 25 (2010) 1402–1407.
[88] G.V. Naik, V.M. Shalaev, A. Boltasseva, Alternative plasmonic materials: beyond gold and silver, Adv. Mater. 25 (2013) 3264–3294.
[89] K. Manthiram, A.P. Alivisatos, Tunable localized surface plasmon resonances in tungsten oxide nanocrystals, J. Am. Chem. Soc. 134 (2012) 3995–3998.
[90] M.R. Mahmoudian, W.J. Basirun, P.M. Woi, M. Sookhakian, R. Yousefi, H. Ghadimi, Y. Alias, Synthesis and characterization of Co3O4 ultra-nanosheets and Co3O4 ultra-nanosheet-Ni(OH)2 as non-enzymatic electrochemical sensors for glucose detection, Mater. Sci. Eng. C 59 (2016) 500–508.
[91] K. Yang, M. Zeng, X. Fu, J. Li, N. Ma, L. Tao, Establishing biodegradable single-layer MnO2 nanosheets as a platform for live cell microRNA sensing, RSC Adv. 5 (2015) 104245–104249.
[92] J. Yuan, Y. Cen, X.-J. Kong, S. Wu, C.-L. Liu, R.-Q. Yu, X. Chu, MnO2-nanosheet-modified upconversion nanosystem for sensitive turn-on fluorescence detection of H2O2 and glucose in blood, ACS Appl. Mater. Interfaces 7 (2015) 10548–10555.
[93] R. Deng, X. Xie, M. Vendrell, Y.-T. Chang, X. Liu, Intracellular glutathione detection using MnO2-nanosheet-modified upconversion nanoparticles, J. Am. Chem. Soc. 133 (2011) 20168–20171.
[94] N. Li, W. Diao, Y. Han, W. Pan, T. Zhang, B. Tang, MnO2-modified persistent luminescence nanoparticles for detection and imaging of glutathione in living cells and in vivo, Chem. – A Eur. J. 20 (2014) 16488–16491.
[95] Y. Wang, K. Jiang, J. Zhu, L. Zhang, H. Lin, A FRET-based carbon dot?MnO2 nanosheet architecture for glutathione sensing in human whole blood samples, Chem. Commun. 51 (2015) 12748–12751.
[96] X. Wang, D. Wang, Y. Guo, C. Yang, X. Liu, A. Iqbal, W. Liu, W. Qin, D. Yan, H. Guo, Fluorescent glutathione probe based on MnO2-phenol formaldehyde resin nanocomposite, Biosens. Bioelectron. 77 (2016) 299–305.
[97] H. Ma, X. Li, X. Liu, M. Deng, X. Wang, A. Iqbal, W. Liu, W. Qin, Fluorescent glutathione probe based on MnO2–Si quantum dots nanocomposite directly used for intracellular glutathione imaging, Sens. Actuators B Chem. 255 (2018) 1687–1693.
[98] X. Tan, L. Wang, C. Cheng, X. Yan, B. Shen, J. Zhang, Plasmonic MoO3-x@MoO3 nanosheets for highly sensitive SERS detection through nanoshell-isolated electromagnetic enhancement, Chem. Commun. 52 (2016) 2893–2896.
[99] S. Yuan, D. Peng, D. Song, J. Gong, Layered titanate nanosheets as an enhanced sensing platform for ultrasensitive stripping voltammetric detection of mercury (II), Sen. Actuators B Chem. 181 (2013) 432–438.
[100] Y.-L.T. Ngo, L.T. Hoa, J.S. Chung, S.H. Hur, Multi-dimensional Ag/NiO/reduced graphene oxide nanostructures for a highly sensitive non-enzymatic glucose sensor, J. Alloys Compd. 712 (2017) 742–751.
[101] J. Yang, M. Cho, C. Pang, Y. Lee, Highly sensitive non-enzymatic glucose sensor based on over-oxidized polypyrrole nanowires modified with Ni(OH)2 nanoflakes, Sens. Actuators B Chem. 211 (2015) 93–101.
[102] X.H. Xia, J.P. Tu, J. Zhang, X.L. Wang, W.K. Zhang, H. Huang, Electrochromic properties of porous NiO thin films prepared by a chemical bath deposition, Sol. Energy Mater. Sol. Cells 92 (2008) 628–633.
[103] P. Lu, Y. Lei, S. Lu, Q. Wang, Q. Liu, Three-dimensional roselike a-Ni(OH)2 assembled from nanosheet building blocks for non-enzymatic glucose detection, Anal. Chim. Acta 880 (2015) 42–51.
[104] P. Lu, Q. Liu, Y. Xiong, Q. Wang, Y. Lei, S. Lu, L. Lu, L. Yao, Nanosheets-assembled hierarchical microstructured Ni(OH)2 hollow spheres for highly sensitive enzyme-free glucose sensors, Electrochim. Acta 168 (2015) 148–156.
[105] H. Yang, G. Gao, F. Teng, W. Liu, S. Chen, Z. Ge, Nickel hydroxide nanoflowers for a nonenzymatic electrochemical glucose sensor, J. Electrochem. Soc. 161 (2014) B216–B219.
[106] K. Xia, C. Yang, Y. Chen, L. Tian, Y. Su, J. Wang, L. Li, In situ fabrication of Ni(OH)2 flakes on Ni foam through electrochemical corrosion as high sensitive and stable binder-free electrode for glucose sensing, Sens. Actuators B Chem. 240 (2017) 979–987.
[107] G.T.S. How, A. Pandikumar, H.N. Ming, L.H. Ngee, Highly exposed {001} facets of titanium dioxide modified with reduced graphene oxide for dopamine sensing, Sci. Rep. 4 (2014) 5044.
[108] P.K. Vabbina, A. Kaushik, N. Pokhrel, S. Bhansali, N. Pala, Electrochemical cortisol immunosensors based on sonochemically synthesized zinc oxide 1D nanorods and 2D nanoflakes, Biosens. Bioelectron. 63 (2015) 124–130.
[109] K. Kalantar-zadeh, J.Z. Ou, T. Daeneke, A. Mitchell, T. Sasaki, M.S. Fuhrer, Two dimensional and layered transition metal oxides, Appl. Mater. Today 5 (2016) 73–89.
[110] P.R. Solanki, A. Kaushik, V.V. Agrawal, B.D. Malhotra, Nanostructured metal oxide-based biosensors, NPG Asia Mater. 3 (2011) 17–24.
[111] S. Marimuthu, Y. Mohamad, Needle-like polypyrrole–NiO composite for non-enzymatic detection of glucose, Synth. Met. 207 (2015) 35–41.
[112] G. Wu, Y.-Z. Fang, S. Yang, J.R. Lupton, N.D. Turner, Glutathione metabolism and its implications for health, J. Nutr. 134 (2004) 489–492.
[113] D. Zhang, G. Li, X. Yang, J.C. Yu, A micrometer-size TiO2 single-crystal photocatalyst with remarkable 80% level of reactive facets, Chem. Commun. 438 (2009) 4381–4383.
[114] J.S. Chen, Y.L. Tan, C.M. Li, Y.L. Cheah, D. Luan, Constructing hierarchical spheres from large ultrathin anatase TiO2 nanosheets with nearly 100% exposed (001) facets for fast reversible lithium storage, J. Am. Chem. Soc. 132 (2010) 6124–6130.
[115] H.-J. Kim, J.-H. Lee, Highly sensitive and selective gas sensors using p-type oxide semiconductors: overview, Sens. Actuators B Chem. 192 (2014) 607–627.
[116] I.-D. Kim, A. Rothschild, H.L. Tuller, Advances and new directions in gas-sensing devices, Acta Mater. 61 (2013) 974–1000.
[117] J. Zhang, Z. Qin, D. Zeng, C. Xie, Metal-oxide-semiconductor based gas sensors: screening, preparation, and integration, Phys. Chem. Chem. Phys. 19 (2017) 6313–6329.
[118] A. Gurlo, R. Riedel, In situ and operando spectroscopy for assessing mechanisms of gas sensing, Angew. Chemie – Int. Ed. 46 (2007) 3826–3848.
[119] R. Azimirad, A.H. Bayani, S. Safa, The effect of concentration of H2 physisorption on the current-voltage characteristic of armchair BN nanotubes in CNT-BNNT-CNT set, Pramana – J. Phys. 87 (2016) 46.
[120] A. Ponzoni, C. Baratto, N. Cattabiani, M. Falasconi, V. Galstyan, E. Nunez-Carmona, F. Rigoni, V. Sberveglieri, G. Zambotti, D. Zappa, Metal oxide gas sensors, a survey of selectivity issues addressed at the SENSOR lab, Brescia (Italy), Sensors 17 (2017) 714.
[121] M. Hübner, C.E. Simion, A. Tomescu-Stănoiu, S. Pokhrel, N. Bârsan, U. Weimar, Influence of humidity on CO sensing with p-type CuO thick film gas sensors, Sens. Actuators B Chem. 153 (2011) 347–353.
[122] H.-R. Kim, A. Haensch, I.-D. Kim, N. Barsan, U. Weimar, J.-H. Lee, The role of NiO doping in reducing the impact of humidity on the performance of SnO2-based gas sensors: synthesis strategies, and phenomenological and spectroscopic studies, Adv. Funct. Mater. 21 (2011) 4456–4463.
[123] J. Zhang, D. Zeng, Q. Zhu, J. Wu, Q. Huang, C. Xie, Effect of nickel vacancies on the room-temperature NO2 sensing properties of mesoporous NiO nanosheets, J. Phys. Chem. C 120 (2016) 3936–3945.
[124] W. Guo, Design of gas sensor based on Fe-doped ZnO nanosheet-spheres for low concentration of formaldehyde detection, J. Electrochem. Soc. 163 (2016) B517–B525.
[125] J. Liu, S. Li, B. Zhang, Y. Wang, Y. Gao, X. Liang, Y. Wang, G. Lu, Flower-like In2O3 modified by reduced graphene oxide sheets serving as a highly sensitive gas sensor for trace NO2 detection, J.Colloid Interface Sci. 504 (2017) 206–213.
[126] Y. Lu, Y. Ma, S. Ma, S. Yan, Hierarchical heterostructure of porous NiO nanosheets on flower-like ZnO assembled by hexagonal nanorods for high-performance gas sensor, Ceram. Int. 43 (2017) 7508–7515.
[127] Q. Wang, X. Li, F. Liu, Y. Sun, C. Wang, X. Li, P. Sun, J. Lin, G. Lu, Three-dimensional flake-flower Co/Sn oxide composite and its excellent ethanol sensing properties, Sens. Actuators B Chem. 230 (2016) 17–24.
[128] Y. Luo, C. Zhang, B. Zheng, X. Geng, M. Debliquy, Hydrogen sensors based on noble metal doped metal-oxide semiconductor: a review, Int. J. Hydrogen Energy 42 (2017) 20386–20397.
[129] D.R. Miller, S.A. Akbar, P.A. Morris, Nanoscale metal oxide-based heterojunctions for gas sensing: a review, Sensors Actuators B Chem. 204 (2014) 250–272.
[130] H.-S. Woo, C.W. Na, J.-H. Lee, Design of highly selective gas sensors via physicochemical modification of oxide nanowires: overview, Sensors 16 (2016) 1531.
[131] Q. Zhao, X. Deng, M. Ding, L. Gan, T. Zhai, X. Xu, One-pot synthesis of Zn-doped SnO2 nanosheet-based hierarchical architectures as a glycol gas sensor and photocatalyst, CrystEngComm 17 (2015) 4394–4401.
[132] L.T. Hoa, H.N. Tien, S.H. Hur, Fabrication of novel 2D NiO nanosheet branched on 1D-ZnO nanorod arrays for gas sensor application, J. Nanomater. 2014 (2014) 710874.
[133] L. Wang, S. Wang, H. Zhang, Y. Wang, J. Yang, W. Huang, Au-functionalized porous ZnO microsheets and their enhanced gas sensing properties, New J. Chem. 38 (2014) 2530–2537.
[134] X. Zhang, P. Guo, Q. Pan, K. Shi, G. Zhang, Novel p-n heterojunction Co3O4/AlOOH composites materials for gas sensing at room temperature, J. Alloys Compd. 727 (2017) 514–521.
[135] J. Xiao, C. Song, W. Dong, Y. Yin, C. Li, Preparation and gas sensing properties of hierarchical flower-shaped Bi2WO6, Aust. J. Chem. 69 (2015) 107–111.

[136] J. Xiao, W. Dong, C. Song, Y. Yu, L. Zhang, C. Li, Y. Yin, Nitrogen oxide gas-sensing characteristics of hierarchical Bi2WO6 microspheres prepared by a hydrothermal method, Mater. Sci. Semicond. Process. 40 (2015) 463–467.
[137] L.-J. Zhou, C. Li, X. Zou, J. Zhao, P.-P. Jin, L.-L. Feng, M.-H. Fan, G.-D. Li, Porous nanoplate-assembled CdO/ZnO composite microstructures: a highly sensitive material for ethanol detection, Sens. Actuators B Chem. 197 (2014) 370–375.
[138] K. Xu, J. Zou, S. Tian, Y. Yang, F. Zeng, T. Yu, Y. Zhang, X. Jie, C. Yuan, Single-crystalline porous nanosheets assembled hierarchical Co3O4 microspheres for enhanced gas-sensing properties to trace xylene, Sens. Actuators B Chem. 246 (2017) 68–77.
[139] S.-J. Hwang, K.-I. Choi, J.-W. Yoon, Y.C. Kang, J.-H. Lee, Pure and palladium-loaded Co3O4 hollow hierarchical nanostructures with giant and ultraselective chemiresistivity to xylene and toluene, Chem. – A Eur. J. 21 (2015) 5872–5878.
[140] H. Che, A. Liu, X. Zhang, J. Hou, J. Mu, H. He, Two-dimensional nanosheets-assembled flower-like Co3O4 microspheres and their gas sensing performances, Nano 9 (2014) 1450071.
[141] K.-I. Choi, H.-R. Kim, K.-M. Kim, D. Liu, G. Cao, J.-H. Lee, C2H5OH sensing characteristics of various Co3O4 nanostructures prepared by solvothermal reaction, Sens. Actuators B Chem. 146 (2010) 183–189.
[142] Z. Zhang, Z. Wen, Z. Ye, L. Zhu, Gas sensors based on ultrathin porous Co3O4 nanosheets to detect acetone at low temperature, RSC Adv. 5 (2015) 59976–59982.
[143] Y. Lin, H. Ji, Z. Shen, Q. Jia, D. Wang, Enhanced acetone sensing properties of Co3O4 nanosheets with highly exposed (111) planes, J. Mater. Sci. Mater. Electron. 27 (2016) 2086–2095.
[144] B. Geng, F. Zhan, C. Fang, N. Yu, A facile coordination compound precursor route to controlled synthesis of Co3O4 nanostructures and their room-temperature gas sensing properties, J. Mater. Chem. 18 (2008) 4977–4984.
[145] H. Deng, H.R. Li, F. Wang, C. Yuan, S. Liu, P. Wang, L. Xie, Y. Sun, F. Chang, A high sensitive and low detection limit of formaldehyde gas sensor based on hierarchical flower-like CuO nanostructure fabricated by sol-gel method, J. Mater. Sci. Mater. Electron. 27 (2016) 6766–6772.
[146] T. Wang, Q. Xiao, Solvothermal synthesis and sensing properties of meso-macroporous hierarchical CuO microspheres composed of nanosheets, Mater. Chem. Phys. 139 (2013) 603–608.
[147] X. Jia, H. Fan, W. Yang, Hydrothermal synthesis and primary gas sensing properties of CuO nanosheets, J. Dispers. Sci. Technol. 31 (2010) 866–869.
[148] F. Zhang, A. Zhu, Y. Luo, Y. Tian, J. Yang, Y. Qin, CuO nanosheets for sensitive and selective determination of H2S with high recovery ability, J. Phys. Chem. C. 114 (2010) 19214–19219.
[149] J. Tan, X. Huang, Ultra-thin nanosheets-assembled hollowed-out hierarchical a-Fe2O3 nanorods: synthesis via an interface reaction route and its superior gas sensing properties, Sens. Actuators B Chem. 237 (2016) 159–166.
[150] Q. Hao, S. Liu, X. Yin, Z. Du, M. Zhang, L. Li, Y. Wang, T. Wang, Q. Li, Flexible morphology-controlled synthesis of mesoporous hierarchical a-Fe2O3 architectures and their gas-sensing properties, CrystEngComm 13 (2011) 806–812.
[151] K. Fan, J. Guo, L. Cha, Q. Chen, J. Ma, Atomic layer deposition of ZnO onto Fe2O3 nanoplates for enhanced H2S sensing, J. Alloys Compd. 698 (2017) 336–340.
[152] Z. D. Wei, L. Huang, X. Wang, S. Chuai, G. Lu Zhang, Hydrothermal synthesis of Ce-doped hierarchical flower-like In2O3 microspheres and their excellent gas-sensing properties, Sens. Actuators B Chem. 255 (2018) 1211–1219.
[153] D. Han, P. Song, H. Zhang, H. Yan, Q. Xu, Z. Yang, Q. Wang, Flower-like In2O3 hierarchical nanostructures: synthesis, characterization, and gas sensing properties, RSC Adv. 4 (2014) 50241–50248.
[154] W.-H. Zhang, W.-D. Zhang, Biomolecule-assisted synthesis and gas-sensing properties of porous nanosheet-based corundum In2O3 microflowers, J. Solid State Chem. 186 (2012) 29–35.
[155] X. Xu, X. Li, H. Zhang, C. Feng, C. Wang, F. Liu, Y. Sun, P. Sun, G. Lu, Synthesis, characterization and gas sensing properties of porous flower-like indium oxide nanostructures, RSC Adv. 5 (2015) 30297–30302.
[156] X. Xu, D. Wang, W. Wang, P. Sun, J. Ma, X. Liang, Y. Sun, Y. Ma, G. Lu, Porous hierarchical In2O3 nanostructures: hydrothermal preparation and gas sensing properties, Sens. Actuators B Chem. 171–172 (2012) 1066–1072.
[157] M. Cai, R. Li, F. Wang, X. Guo, Q. Bai, L. Sun, X. Han, Architecture of designed hollow indium oxide microspheres assembled by porous nanosheets with high gas sensing capacity, J. Alloys Compd. 729 (2017) 222–230.
[158] X. Wang, J. Su, H. Chen, G.-D. Li, Z. Shi, H. Zou, X. Zou, Ultrathin In2O3 nanosheets with uniform mesopores for highly sensitive nitric oxide detection, ACS Appl. Mater. Interfaces 9 (2017) 16335–16342.
[159] H. Sun, Z. Chu, D. Hong, G. Zhang, Y. Xie, L. Li, K. Shi, Three-dimensional hierarchical flower-like Mg-Al-layered double hydroxides: fabrication, characterization and enhanced sensing properties to NOx at room temperature, J. Alloys Compd. 658 (2016) 561–568.
[160] A. Sanger, A. Kumar, A. Kumar, R. Chandra, Highly sensitive and selective hydrogen gas sensor using sputtered grown Pd decorated MnO2 nanowalls, Sensors Actuators B Chem. 234 (2016) 8–14.
[161] X. Tian, L. Yang, X. Qing, K. Yu, X. Wang, Trace level detection of hydrogen gas using birnessite-type manganese oxide, Sens. Actuators B Chem. 207 (2015) 34–42.
[162] Y. Liu, W. Zeng, Facile synthesis of 3D flower-like MoO3 and its gas sensor application, J. Mater. Sci. Mater. Electron. 27 (2016) 12996–13001.
[163] F. Ji, X. Ren, X. Zheng, Y. Liu, L. Pang, J. Jiang, S. (Frank) Liu, 2D-MoO3 nanosheets for superior gas sensors, Nanoscale 8 (2016) 8696–8703.
[164] M.M.Y.A. Alsaif, S. Balendhran, M.R. Field, K. Latham, W. Wlodarski, J.Z. Ou, K. Kalantar-zadeh, Two dimensional a-MoO3 nanoflakes obtained using solvent-assisted grinding and sonication method: application for H2 gas sensing, Sens. Actuators B Chem. 192 (2014) 196–204.
[165] D. Hong, J. Zhang, A.U. Rehman, L. Gong, J. Zhou, K. Kan, L. Li, K. Shi, One-step synthesis of hierarchical Ni-Fe-Al layered double hydroxide with excellent sensing properties for NOx at room temperature, RSC Adv. 6 (2016) 103192–103198.
[166] Y. Zhang, W. Zeng, New insight into gas sensing performance of nanoneedle-assembled and nanosheet-assembled hierarchical NiO nanoflowers, Mater. Lett. 195 (2017) 217–219.
[167] S. Liu, W. Zeng, T. Chen, Synthesis of hierarchical flower-like NiO and the influence of surfactant, Phys. E 85 (2017) 13–18.
[168] R. Miao, W. Zeng, Hydrothermal synthesis of flake-flower NiO architectures: structure, growth and gas-sensing properties, Mater. Lett. 171 (2016) 200–203.
[169] H. Gao, D. Wei, P. Lin, C. Liu, P. Sun, K. Shimanoe, N. Yamazoe, G. Lu, The design of excellent xylene gas sensor using Sn-doped NiO hierarchical nanostructure, Sensors Actuators B Chem. 253 (2017) 1152–1162.
[170] C. Wang, X. Cheng, X. Zhou, P. Sun, X. Hu, K. Shimanoe, G. Lu, N. Yamazoe, Hierarchical a-Fe2O3/NiO composites with a hollow structure for a gas sensor, ACS Appl. Mater. Interfaces 6 (2014) 12031–12037.
[171] G. Zhu, Y. Liu, C. Xi, C. Bao, H. Xu, X. Shen, X. Zhu, Polymer guided synthesis of Ni(OH)2 with hierarchical structure and their application as the precursor for sensing materials, CrystEngComm 15 (2013) 9189.
[172] C. Zhao, J. Fu, Z. Zhang, E. Xie, Enhanced ethanol sensing performance of porous ultrathin NiO nanosheets with neck-connected networks, RSC Adv. 3 (2013) 4018–4023.
[173] H.-J. Kim, J.-W. Yoon, K.-I. Choi, H.W. Jang, A. Umar, J.-H. Lee, Ultraselective and sensitive detection of xylene and toluene for monitoring indoor air pollution using Cr-doped NiO hierarchical nanostructures, Nanoscale 5 (2013) 7066–7073.
[174] K. Tian, X.-X. Wang, H.-Y. Li, R. Nadimicherla, X. Guo, Lotus pollen derived 3-dimensional hierarchically porous NiO microspheres for NO2 gas sensing, Sens. Actuators B Chem. 227 (2016) 554–560.
[175] L. Lin, T. Liu, B. Miao, W. Zeng, Hydrothermal fabrication of uniform hexagonal NiO nanosheets: structure, growth and response, Mater. Lett. 102–103 (102) (2013) 43—.
[176] S. Wang, D. Huang, S. Xu, W. Jiang, T. Wang, J. Hu, N. Hu, Y. Su, Y. Zhang, Z. Yang, Two-dimensional NiO nanosheets with enhanced room temperature NO2 sensing performance via Al doping, Phys. Chem. Chem. Phys. 19 (2017) 19043–19049.
[177] G. Li, X. Wang, H. Ding, T. Zhang, A facile synthesis method for Ni(OH)2 ultrathin nanosheets and their conversion to porous NiO nanosheets used for formaldehyde sensing, RSC Adv. 2 (2012) 13018–13023.
[178] N.D. Hoa, S.A. El-Safty, Synthesis of mesoporous NiO nanosheets for the detection of toxic NO2 gas, Chem. – A Eur. J. 17 (2011) 12896–12901.
[179] C. Wang, W. Zeng, T. Chen, Facile synthesis of thin nanosheet assembled flower-like NiO-ZnO composite and its ethanol-sensing performance, J. Mater. Sci. Mater. Electron. 28 (2017) 222–227.
[180] M. Bao, Y. Chen, F. Li, J. Ma, T. Lv, Y. Tang, L. Chen, Z. Xu, T. Wang, Plate-like p–n heterogeneous NiO/WO3 nanocomposites for high performance room temperature NO2 sensors, Nanoscale 6 (2014) 4063–4066.
[181] Y. Liu, Y. Jiao, Z. Zhang, F. Qu, A. Umar, X. Wu, Hierarchical SnO2 nanostructures made of intermingled ultrathin nanosheets for environmental remediation smart gas sensor, and supercapacitor applications, ACS Appl. Mater. Interfaces 6 (2014) 2174–2184.
[182] J. Tian, J. Wang, Y. Hao, H. Du, X. Li, Toluene sensing properties of porous Pd-loaded flower-like SnO2 microspheres, Sens. Actuators B Chem. 202 (2014) 795–802.
[183] J. Hu, Y. Wang, W. Wang, Y. Xue, P. Li, K. Lian, L. Chen, W. Zhang, S. Zhuiykov, Enhancement of the acetone sensing capabilities to ppb detection level by Fe-doped three-dimensional SnO2 hierarchical microstructures fabricated via a hydrothermal method, J. Mater. Sci. 52 (2017) 11554–11568.
[184] C. Wang, W. Zeng, New insights into multi-hierarchical nanostructures with size-controllable blocking units for their gas sensing performance, J. Mater. Sci. Mater. Electron. 28 (2017) 10847–10852.
[185] Y. Li, T. Liu, H. Zhang, New insight into gas sensing performance of nanoneedle-assembled and nanosheet-assembled hierarchical SnO2 structures, Mater. Lett. 176 (2016) 9–12.
[186] W.X. Jin, S.Y. Ma, Z.Z. Tie, J.J. Wei, J. Luo, X.H. Jiang, T.T. Wang, W.Q. Li, L. Cheng, Y.Z. Mao, One-step synthesis and highly gas-sensing properties of hierarchical Cu-doped SnO2 nanoflowers, Sens. Actuators B Chem. 213 (2015) 171–180.
[187] W.X. Jin, S.Y. Ma, A.M. Sun, J. Luo, L. Cheng, W.Q. Li, Z.Z. Tie, X.H. Jiang, T.T. Wang, Synthesis of hierarchical SnO2 nanoflowers and their high gas-sensing properties, Mater. Lett. 143 (2015) 283–286.
[188] H. Zhang, W. Zeng, J. Hao, Y. Li, B. Miao, Hydrothermal synthesis of flower-like SnO2 architectures with superior gas sensing properties, Mater. Lett. 145 (2015) 133–136.
[189] L. Cheng, S.Y. Ma, T.T. Wang, J. Luo, Synthesis and enhanced acetone sensing properties of 3D porous flower-like SnO2 nanostructures, Mater. Lett. 143 (2015) 84–87.
[190] W. Zhang, W. Zeng, B. Miao, Z. Wang, Effect of the sheet thickness of hierarchical SnO2 on the gas sensing performance, Appl. Surf. Sci. 355 (2015) 631–637.
[191] X. Kuang, T. Liu, W. Wang, S. Hussain, X. Peng, Controlled synthesis of SnO2 hierarchical architectures made of ultrathin nanoflakes for enhanced ethanol gas sensing properties, Appl. Surf. Sci. 351 (2015) 1087–1093.
[192] X.H. Jiang, S.Y. Ma, A.M. Sun, Z.M. Zhang, W.X. Jin, T.T. Wang, W.Q. Li, X.L. Xu, J. Luo, L. Cheng, Y.Z. Mao, M. Zhang, Hydrothermal self-assembly of novel porous flower-like SnO2 architecture and its application in ethanol sensor, Appl. Surf. Sci. 355 (2015) 1192–1200.

[193] W.X. Jin, S.Y. Ma, Z.Z. Tie, W.Q. Li, J. Luo, L. Cheng, X.L. Xu, T.T. Wang, X.H. Jiang, Y.Z. Mao, Synthesis of hierarchical SnO2 nanoflowers with enhanced acetic acid gas sensing properties, Appl. Surf. Sci. 353 (2015) 71–78.
[194] Q. Zhao, D. Ju, X. Deng, J. Huang, B. Cao, X. Xu, Morphology-modulation of SnO2 hierarchical architectures by Zn doping for glycol gas sensing and photocatalytic applications, Sci. Rep. 5 (2015) 7874.
[195] H. Chen, Q. Wang, C. Kou, Y. Sui, Y. Zeng, F. Du, One-pot synthesis and improved sensing properties of hierarchical flowerlike SnO2 assembled from sheet and ultrathin rod subunits, Sens. Actuators B Chem. 194 (2014) 447–453.
[196] Y. Guan, D. Wang, X. Zhou, P. Sun, H. Wang, J. Ma, G. Lu, Hydrothermal preparation and gas sensing properties of Zn-doped SnO2 hierarchical architectures, Sens. Actuators B Chem. 191 (2014) 45–52.
[197] L. Wang, S. Wang, Y. Wang, H. Zhang, Y. Kang, W. Huang, Synthesis of hierarchical SnO2 nanostructures assembled with nanosheets and their improved gas sensing properties, Sens. Actuators B Chem. 188 (2013) 85–93.
[198] W. Zeng, Q. He, K. Pan, Y. Wang, Synthesis of multifarious hierarchical flower-like SnO2 and their gas-sensing properties, Phys. E 54 (2013) 313–318.
[199] Y. Zeng, Y. Bing, C. Liu, W. Zheng, G. Zou, Self-assembly of hierarchical ZnSnO3-SnO2 nanoflakes and their gas sensing properties, Trans. Nonferrous Met. Soc. China. 22 (2012) 2451–2458.
[200] P. Sun, W. Zhao, Y. Cao, Y. Guan, Y. Sun, G. Lu, Porous SnO2 hierarchical nanosheets: hydrothermal preparation, growth mechanism, and gas sensing properties, CrystEngComm 13 (2011) 3718–3724.
[201] J. Guo, J. Zhang, H. Gong, D. Ju, B. Cao, Au nanoparticle-functionalized 3D SnO2 microstructures for high performance gas sensor, Sens. Actuators B Chem. 226 (2016) 266–272.
[202] L. Liu, P. Song, Q. Wei, X. Zhong, Z. Yang, Q. Wang, Synthesis of porous SnO2 hexagon nanosheets loaded with Au nanoparticles for high performance gas sensors, Mater. Lett. 201 (2017) 211–215.
[203] S. Cao, W. Zeng, Z. Zhu, X. Peng, Synthesis of SnO2 nanostructures from 1D to 3D via a facile hydrothermal method and their gas sensing properties, J. Mater. Sci. Mater. Electron. 26 (2015) 1820–1826.
[204] M.-H. Xu, F.-S. Cai, J. Yin, Z.-H. Yuan, L.-J. Bie, Facile synthesis of highly ethanol-sensitive SnO2 nanosheets using homogeneous precipitation method, Sensors Actuators B Chem. 145 (2010) 875–878.
[205] Z. Lou, L. Wang, R. Wang, T. Fei, T. Zhang, Synthesis and ethanol sensing properties of SnO2 nanosheets via a simple hydrothermal route, Solid. State. Electron. 76 (2012) 91–94.
[206] P. Sun, Y. Cao, J. Liu, Y. Sun, J. Ma, G. Lu, Dispersive SnO2 nanosheets: hydrothermal synthesis and gas-sensing properties, Sens. Actuators B Chem. 156 (2011) 779–783.
[207] X.H. Yang, H. Xie, H.T. Fu, X.Z. An, X.C. Jiang, A.B. Yu, Synthesis of hierarchical nanosheet-assembled V2O5 microflowers with high sensing properties towards amines, RSC Adv. 6 (2016) 87649–87655.
[208] X. Rui, Z. Lu, Z. Yin, D.H. Sim, N. Xiao, T.M. Lim, H.H. Hng, H. Zhang, Q. Yan, Oriented molecular attachments through sol-gel chemistry for synthesis of ultrathin hydrated vanadium pentoxide nanosheets and their applications, Small 9 (2013) 716–721.
[209] W. Zeng, H. Zhang, Z. Wang, Effects of different petal thickness on gas sensing properties of flower-like WO3. H2O hierarchical architectures, Appl. Surf. Sci. 347 (2015) 73–78.
[210] Z. Liu, B. Liu, W. Xie, H. Li, R. Zhou, Q. Li, T. Wang, Enhanced selective acetone sensing characteristics based on Co-doped WO3 hierarchical flower-like nanostructures assembled with nanoplates, Sens. Actuators B Chem. 235 (2016) 614–621.
[211] S. Wei, Y. Xing, Y. Li, Y. Zhao, W. Du, M. Zhou, Preparation and gas sensing properties of flower-like WO3 hierarchical architecture, Vacuum 129 (2016) 13–19.
[212] Y. Yu, W. Zeng, H. Zhang, Hydrothermal synthesis of assembled WO3. H2O nanoflowers with enhanced gas sensing performance, Mater. Lett. 171 (2016) 162–165.
[213] D. Meng, G. Wang, X. San, Y. Song, Y. Shen, Y. Zhang, K. Wang, F. Meng, Synthesis of WO3 flower-like hierarchical architectures and their sensing properties, J. Alloys Compd. 649 (2015) 731–738.
[214] C.-S. Wu, Hydrothermal fabrication of WO3 hierarchical architectures: structure, growth and response, Nanomaterials 5 (2015) 1250–1255.
[215] J. Li, X. Liu, J. Cui, J. Sun, Hydrothermal synthesis of self-assembled hierarchical tungsten oxides hollow spheres and their gas sensing properties, ACS Appl. Mater. Interfaces 7 (2015) 10108–10114.
[216] C. Wang, X. Li, C. Feng, Y. Sun, G. Lu, Nanosheets assembled hierarchical flower-like WO3 nanostructures: synthesis, characterization, and their gas sensing properties, Sens. Actuators B Chem. 210 (2015) 75–81.
[217] C. Wang, R. Sun, X. Li, Y. Sun, P. Sun, F. Liu, G. Lu, Hierarchical flower-like WO3 nanostructures and their gas sensing properties, Sens. Actuators B Chem. 204 (2014) 224–230.
[218] W. Zeng, Y. Li, H. Zhang, Hierarchical WO3 porous microspheres and their sensing properties, J. Mater. Sci. Mater. Electron. 25 (2014) 1512–1516.
[219] W. Zeng, Y. Li, B. Miao, K. Pan, Hydrothermal synthesis and gas sensing properties of WO3. H2O with different morphologies, Phys. E 56 (2014) 183–188.
[220] B. Xiao, Q. Zhao, C. Xiao, T. Yang, P. Wang, F. Wang, X. Chen, M. Zhang, Low-temperature solvothermal synthesis of hierarchical flower-like WO3 nanostructures and their sensing properties for H2S, CrystEngComm 17 (2015) 5710–5716.
[221] T. Yang, H. Tian, Y. Zhang, C. Li, Chemical stability of 2D-nanostructured WO3 in hydrogen sensing under varied operation temperature, Nano 11 (2016) 1650092.
[222] M.B. Rahmani, M.H. Yaacob, Y.M. Sabri, Hydrogen sensors based on 2D WO3 nanosheets prepared by anodization, Sen. Actuators B Chem. 251 (2017) 57–64.
[223] Z. Wang, D. Wang, J. Sun, Controlled synthesis of defect-rich ultrathin two-dimensional WO3 nanosheets for NO2 gas detection, Sens. Actuators B Chem. 245 (2017) 828–834.
[224] M. Breedon, P. Spizzirri, M. Taylor, J. du Plessis, D. McCulloch, J. Zhu, Z. Yu, C. Rix, W. Wlodarski, K. Kalantar-zadeh, Synthesis of nanostructured tungsten oxide thin films: a simple, controllable, inexpensive, aqueous sol-gel method, Cryst. Growth Des. 10 (2010) 430–439.
[225] A. Boudiba, C. Zhang, C. Bittencourt, P. Umek, M.-G. Olivier, R. Snyders, M. Debliquy, Hydrothermal synthesis of two dimensional WO3 nanostructures for NO2 detection in the ppb-level, Procedia Eng. 47 (2012) 228–231.
[226] S.S. Kalanur, J. Heo, I.-H. Yoo, H. Seo, 2-D WO3 decorated with Pd for rapid gasochromic and electrical hydrogen sensing, Int. J. Hydrogen Energy 42 (2017) 16901–16908.
[227] X. Xie, X. Wang, J. Tian, X. Song, N. Wei, H. Cui, Growth of porous ZnO single crystal hierarchical architectures with ultrahigh sensing performances to ethanol and acetone gases, Ceram. Int. 43 (2017) 1121–1128.
[228] C. Peng, J. Guo, W. Yang, C. Shi, M. Liu, Y. Zheng, J. Xu, P. Chen, T. Huang, Y. Yang, Synthesis of three-dimensional flower-like hierarchical ZnO nanostructure and its enhanced acetone gas sensing properties, J. Alloys Compd. 654 (2016) 371–378.
[229] L. Zhang, J. Zhao, H. Lu, L. Li, J. Zheng, J. Zhang, H. Li, Z. Zhu, Highly sensitive and selective dimethylamine sensors based on hierarchical ZnO architectures composed of nanorods and nanosheet-assembled microspheres, Sens. Actuators B Chem. 171–172 (2012) 1101–1109.
[230] Z. Lin, F. Guo, C. Wang, X. Wang, K. Wang, Y. Qu, Preparation and sensing properties of hierarchical 3D assembled porous ZnO from zinc hydroxide carbonate, RSC Adv. 4 (2014) 5122–5129.
[231] X. Liu, J. Zhang, T. Yang, L. Wang, Y. Kang, S. Wang, S. Wu, Self-assembled hierarchical flowerlike ZnO architectures and their gas-sensing properties, Powder Technol. 217 (2012) 238–244.
[232] L. Zhang, J. Zhao, H. Lu, L. Li, J. Zheng, H. Li, Z. Zhu, Facile synthesis and ultrahigh ethanol response of hierarchically porous ZnO nanosheets, Sens. Actuators B Chem. 161 (2012) 209–215.
[233] M. Chen, Z. Wang, D. Han, F. Gu, G. Guo, High-sensitivity NO2 gas sensors based on flower-like and tube-like ZnO nanomaterials, Sens. Actuators B Chem. 157 (2011) 565–574.
[234] P.-Y. Qiao, L.-X. Zhang, M.-Y. Zhu, Y.-Y. Yin, Z.-W. Zhao, H.-N. Sun, J.-Y. Dong, L.-J. Bie, Acetylene sensing enhancement of mesoporous ZnO nanosheets with morphology and defect induced structural sensitization, Sens. Actuators B Chem. 250 (2017) 189–197.
[235] W. Guo, T. Liu, H. Zhang, R. Sun, Y. Chen, W. Zeng, Z. Wang, Gas-sensing performance enhancement in ZnO nanostructures by hierarchical morphology, Sens. Actuators B Chem. 166–167 (2012) 492–499.
[236] A.S.M. Iftekhar Uddin, K.-W. Lee, G.-S. Chung, Acetylene gas sensing properties of an Ag-loaded hierarchical ZnO nanostructure-decorated reduced graphene oxide hybrid, Sens. Actuators B Chem. 216 (2015) 33–40.
[237] M.R. Alenezi, T.H. Alzanki, A.M. Almeshal, A.S. Alshammari, M.J. Beliatis, S.J. Henley, S.R.P. Silva, Hierarchically designed ZnO nanostructure based high performance gas sensors, RSC Adv. 4 (2014) 49521–49528.
[238] Z. Jing, J. Zhan, Fabrication and gas-sensing properties of porous ZnO nanoplates, Adv. Mater. 20 (2008) 4547–4551.
[239] R. Zhang, L. Wang, J. Deng, T. Zhou, Z. Lou, T. Zhang, Hierarchical structure with heterogeneous phase as high performance sensing materials for trimethylamine gas detecting, Sens. Actuators B Chem. 220 (2015) 1224–1231.
[240] G. Zhu, Y. Liu, H. Xu, Y. Chen, X. Shen, Z. Xu, Photochemical deposition of Ag nanocrystals on hierarchical ZnO microspheres and their enhanced gas-sensing properties, CrystEngComm 14 (2012) 719–725.
[241] X. Liu, J. Zhang, L. Wang, T. Yang, X. Guo, S. Wu, S. Wang, 3D hierarchically porous ZnO structures and their functionalization by Au nanoparticles for gas sensors, J. Mater. Chem. 21 (2011) 349–356.
[242] J. Li, H. Fan, X. Jia, Multilayered ZnO nanosheets with 3D porous architectures: synthesis and gas sensing application, J. Phys. Chem. C 114 (2010) 14684–14691.
[243] L. Yu, F. Guo, S. Liu, B. Yang, Y. Jiang, L. Qi, X. Fan, Both oxygen vacancies defects and porosity facilitated NO2 gas sensing response in 2D ZnO nanowalls at room temperature, J. Alloys Compd. 682 (2016) 352–356.
[244] Y. Zhu, Y. Wang, G. Duan, H. Zhang, Y. Li, G. Liu, L. Xu, W. Cai, In situ growth of porous ZnO nanosheet-built network film as high-performance gas sensor, Sens. Actuators B Chem. 221 (2015) 350–356.
[245] L. Yu, J. Wei, Y. Luo, Y. Tao, M. Lei, X. Fan, W. Yan, P. Peng, Dependence of Al3+ on the growth mechanism of vertical standing ZnO nanowalls and their NO2 gas sensing properties, Sens. Actuators B Chem. 204 (2014) 96–101.
[246] L. Yu, F. Guo, Z. Liu, S. Liu, B. Yang, M.-L. Yin, X. Fan, Facile synthesis of three dimensional porous ZnO films with mesoporous walls and gas sensing properties, Mater. Charact. 112 (2016) 224–228.
[247] X.-L. Cheng, Z. Rong, X.-F. Zhang, Y.-M. Xu, S. Gao, H. Zhao, L.-H. Huo, In situ assembled ZnO flower sensors based on porous nanofibers for rapid ethanol sensing, Sens. Actuators B Chem. 188 (2013) 425–432.
[248] Y. Al-Hadeethi, A. Umar, S.H. Al-Heniti, R. Kumar, S.H. Kim, X. Zhang, 2D Sn-doped ZnO ultrathin nanosheet networks for enhanced acetone gas sensing application, Ceram. Int. 43 (2017) 2418–2423.
[249] E. Modaresinezhad, S. Darbari, Realization of a room-temperature/self-powered humidity sensor, based on ZnO nanosheets, Sens. Actuators B Chem. 237 (2016) 358–366.
[250] D. Ju, H. Xu, J. Zhang, J. Guo, B. Cao, Direct hydrothermal growth of ZnO nanosheets on electrode for ethanol sensing, Sens. Actuators B Chem. 201 (2014)

444–451.
[251] F. Fan, P. Tang, Y. Wang, Y. Feng, A. Chen, R. Luo, D. Li, Facile synthesis and gas sensing properties of tubular hierarchical ZnO self-assembled by porous nanosheets, Sens. Actuators B Chem. 215 (2015) 231–240.
[252] J. Zhou, F. Gong, H. Wang, Y. Xiao, F. Li, W. Mai, 3D mace-like hierarchical ZnO nanoarchitecture constructed with microrod bundles and porous single-crystalline nanosheets for acetone sensors with enhanced performances, Mater. Sci. Eng. B. 225 (2017) 68–74.
[253] J. Liu, Z. Guo, F. Meng, T. Luo, M. Li, J. Liu, Novel porous single-crystalline ZnO nanosheets fabricated by annealing ZnS(en)0.5 (en = ethylenediamine) precursor. Application in a gas sensor for indoor air contaminant detection, Nanotechnology 20 (2009) 125501.
[254] Y. Xiao, L. Lu, A. Zhang, Y. Zhang, L. Sun, L. Huo, F. Li, Highly enhanced acetone sensing performances of porous and single crystalline ZnO nanosheets: high percentage of exposed (100) facets working together with surface modification with Pd nanoparticles, ACS Appl. Mater. Interfaces. 4 (2012) 3797–3804.
[255] M. Ali, C.Y. Wang, C.-C. Röhlig, V. Cimalla, T. Stauden, O. Ambacher, NOx sensing properties of In2O3 thin films grown by MOCVD, Sens. Actuators B Chem. 129 (2008) 467–472.
[256] T. Takada, K. Suzuki, M. Nakane, Highly sensitive ozone sensor, Sens. Actuators B Chem. 13–14 (1993) 404–407.
[257] A. Kusior, M. Radecka, L. Zych, K. Zakrzewska, A. Reszka, B.J. Kowalski, Sensitization of TiO2/SnO2 nanocomposites for gas detection, Sens. Actuators B Chem. 189 (2013) 251–259.
[258] X. Wang, Y. Sang, D. Wang, S. Ji, H. Liu, Enhanced gas sensing property of SnO2 nanoparticles by constructing the SnO2-TiO2 nanobelt heterostructure, J. Alloys Compd. 639 (2015) 571–576.
[259] S. Tian, D. Zeng, X. Peng, S. Zhang, C. Xie, Processing-microstructure-property correlations of gas sensors based on ZnO nanotetrapods, Sens. Actuators B Chem. 181 (2013) 509–517.
[260] Y. Zhou, Y. Jiang, T. Xie, H. Tai, G. Xie, A novel sensing mechanism for resistive gas sensors based on layered reduced graphene oxide thin films at room temperature, Sens. Actuators B Chem. 203 (2014) 135–142.
[261] A.P. Lee, B.J. Reedy, Temperature modulation in semiconductor gas sensing, Sens. Actuators B Chem. 60 (1999) 35–42.
[262] F. Röck, N. Barsan, U. Weimar, Electronic nose: current status and future trends, Chem. Rev. 108 (2008) 705–725.
[263] R. Zhang, W. Pang, Z. Feng, X. Chen, Y. Chen, Q. Zhang, H. Zhang, C. Sun, J.J. Yang, D. Zhang, Enabling selectivity and fast recovery of ZnO nanowire gas sensors through resistive switching, Sens. Actuators B Chem. 238 (2017) 357–363.
[264] P. Uthirakumar, S. Muthulingam, R. Khan, J.H. Yun, H.-S. Cho, I.-H. Lee, Surfactant-free synthesis of leaf-like hierarchical CuO nanosheets as a UV light filter, Mater. Lett. 156 (2015) 191–194.
[265] D. Kato, M. Kunitake, M. Nishizawa, T. Matsue, F. Mizutani, Amperometric nitric oxide microsensor using two-dimensional cross-linked Langmuir-Blodgett films of polysiloxane copolymer, Sens. Actuators B Chem. 108 (2005) 384–388.
[266] D. Kato, M. Kunitake, M. Nishizawa, T. Matsue, F. Mizutani, Electrochemical nitric oxide microsensors based on two-dimensional cross-linked polymeric LB films of oligo(dimethylsiloxane) copolymer, Electrochim. Acta. 51 (2005) 938–942.
[267] P. Tarttelin Hernández, S.M.V. Hailes, I.P. Parkin, Hydrocarbon detection with metal oxide semiconducting gas sensors modified by overlayer or admixture of zeolites Na-A, H-Y and H-ZSM-5, Sens. Actuators B Chem. 242 (2017) 1281–1295.
[268] J.N. Anker, W.P. Hall, O. Lyandres, N.C. Shah, J. Zhao, R.P. van Duyne, Biosensing with plasmonic nanosensors, Nat. Mater. 7 (2008) 442–453.

Dr. Petra Dral obtained her Master of Science degree in Chemical Engineering cum laude at the University of Twente, The Netherlands, with a focus on molecules and materials and a special interest in metal oxide nanosheets. She then obtained her PhD degree under the supervision of Professor Johan ten Elshof on the topic of water sensitivity and microporosity in organosilica glasses. Currently she is working as a materials and process engineer in industry.

Dr. Johan E. ten Elshof is professor of Inorganic & Hybrid Nanomaterials Chemistry at the MESA+ Institute for Nanotechnology at the University of Twente in Enschede, Netherlands. His research focuses on the development of novel metal oxide & organic-inorganic nanomaterials, nanopatterns and nanostructures from colloidal and chemical solutions, with specific emphasis on low-dimensional materials like flexible ceramic nanofibers, metal oxide nanosheets and oxide nanowires, and with main application areas in the fields of energy materials and nanoelectronics.